Structural Mechanism of Prestin-Membrane Mechanotransduction

Navid Bavi[1,2,3*⊥], Patrick R Haller[1,3⊥], Kazuaki Homma[3,4,5], Xiaoxuan Lin[1], Wieslawa Milewski[1,3], Minglei Zhao[1], Tobin Sosnick[1,3], and Eduardo Perozo[1,3,6*]

[1] *Department of Biochemistry and Molecular Biology. The University of Chicago. Chicago, IL 60637.*
[2] *Department of Physiology, David Geffen School of Medicine, UCLA, Los Angeles, CA, USA*
[3] *Center for Mechanical Excitability, The University of Chicago. Chicago, IL 60637.*
[4] *Department of Otolaryngology - Head and Neck Surgery, Feinberg School of Medicine, Northwestern University, Chicago, IL 60611, USA*
[5] *The Hugh Knowles Center for Clinical and Basic Science in Hearing and Its Disorders, Northwestern University, Evanston, IL 60608, USA*
[6] *Grossman Institute for Neuroscience, Quantitative Biology and Human Behavior, The University of Chicago, Chicago IL 60637*

[*]Corresponding author. Email: nbavi@mednet.ucla.edu; eperozo@uchicago.edu

[⊥] These authors contributed equally to this manuscript.

Abstract

The motor protein prestin is responsible for the electromotive behavior of outer hair cells (OHCs), which is essential for the sound amplification process in the cochlea[1-3]. Previous studies have shown unequivocally that prestin exhibits piezoelectricity in the plasma membrane[14]. However, the mechanism by which prestin converts sound-elicited receptor potential changes into mechanical movement remains unclear. This electromechanical process entails thinning and thickening of the cell membrane, which reciprocally affects prestin's motor function[4,5]. To model membrane thinning during OHC elongation, we determined multiple high-resolution structures of dolphin prestin in lipid nanodiscs of varying thicknesses using single particle cryo-electron microscopy. Membrane thinning triggered a conformational transition in prestin from the compact "Sensor Up" state to the expanded "Sensor Down" state. Combined with four mutant structures, hydrogen-deuterium exchange mass spectromtery, and patch-clamp electrophysiology, we investigated the structural dynamics of prestin's response to mechanical force stemming from the membrane. By contrasting dolphin prestin with novel structures of lizard SLC26A5 (an anion exchanger), we demonstrate how, driven by the force-from-lipids principle, prestin's motor function is distinct from nonmammalian transporter SLC26A5. Our data suggests that the anion is an inseparable part of the electromotile dolphin prestin anion binding pocket (voltage sensor), which facilitates core-gate interactions in response to mechanical stress. These structural insights offer a high-resolution understanding of how prestin translates membrane tension into charge and motor movement during sound-evoked vibrations, revealing its piezoelectric reciprocal mechanosensing as an essential property in cochlear amplification.

Main

Mechanosensitive proteins are essential for processes ranging from sensory perception to cellular homeostasis[6,7]. Motor prestin (SLC26A5) fulfills all the criteria for being a mechanosensitive protein, as it is abundantly expressed in outer hair cells (OHCs) housed in the mechanosensory organ, the organ of Corti [1,8-10] , and transduces electrical signals (sound-elicited receptor potential changes) into mechanical responses, a process referred to as electromolity[11] that is essential for normal hearing[2,3,12,13]. This electromechanical transduction is bidirectional due to the piezoelectric characteristics of prestin[14], accounting for prestin's sensitivity to membrane thickness/tension[4,5,9,15-17]. Heterologous expression of prestin also confers electromotility and mechanosensitivity on non-auditory cells[1]; however, the molecular mechanisms by which prestin integrates mechanical cues, lipid interactions, and anion binding to modulate its electromechanical activity remain elusive.

Prestin's bell-shaped nonlinear capacitance (NLC) serves as a hallmark of its electromechanical activity, reflecting voltage-dependent transitions between its conformational states[8,9,18-20]. Binding of anions, such as Cl^- and salicylate, significantly influences NLC, underscoring the importance of anion interactions in prestin's function[18,21-25]. While recent high-resolution structures of prestin have provided invaluable insights into its voltage sensing mechanism and in-plane areal expansion[26-29], the precise molecular basis by which mechanical forces influence its charge-transfer properties, and the dynamics of bound anions remains poorly understood.

In this study, we demonstrate how electromotile prestin adheres to the "force-from-lipids" principle[6,30], extending this concept from mechanosensitive ion channels to a membrane motor protein. Using single-particle cryo-electron microscopy (cryo-EM), we resolve ten distinct structures, all in the presence of the physiological anion Cl^-, to systematically dissect prestin's conformational cycle. In combination with functional assays, and hydrogen-deuterium exchange mass spectrometry (HDX-MS)[24], we identify the gate domain of the motor (particularly the TM6-7 region, "electromotility elbow") as a key mechanosensory element and elucidate how the lipid environment modulates prestin's mechanical and electrical states. Moreover, we uncover the role of anion interactions in electromechanical coupling and shed light on the functional adaptations that distinguish electromotile prestin from a closely related transporter counterpart.

Conformational changes in motor prestin due to membrane thickness

To investigate how lipid composition influences prestin's conformational states, we combined electrophysiological and structural approaches. Specifically, we used dolphin (*Tursiops truncatus*)[31,32] prestin as a model for electromotile prestin, as this ortholog is ~94% identical to human prestin, and we've previously shown that it behaves well for structural studies and functional characterization in heterologous systems[26]. Using whole-cell patch-clamp electrophysiology on HEK293 cells overexpressing dolphin prestin, we demonstrated that membrane thickness, dictated by lipid composition, significantly modulates prestin's NLC, similar to previous reports[15,17] albeit with higher effectivity (**Fig. 1a,b**). Bilayer thickness was modulated using α-cyclodextrin, which facilitates lipid exchange with cellular membranes (see Methods for detailed lipid doping protocols). Incorporation of phospholipids with short acyl chains (PC14:1; ie thin lipids) induced a depolarizing shift in the voltage at peak capacitance (V_{pk}) from -58.7 ± 3.0 mV to +61.9 ± 21.0 mV, mimicking membrane thinning during somatic elongation of OHCs. Conversely, incorporation of phospholipids with long acyl chains (PC20:1; i.e., thick lipids), caused a hyperpolarizing shift in V_{pk} to -93.6 ± 4.2, corresponding to membrane thickening during OHC contraction. These shifts in V_{pk} were paralleled by changes in linear capacitance, reinforcing that membrane thickness directly influences prestin's charge transfer and electromotility.

Following up on these functional assays, we conducted single-particle cryo-EM studies to provide structural correlates for the observed functional changes. Of note, the structures reported in this paper are in the presence of Cl^- rather than non-physiological anions (e.g., SO_4^{2-}) to prevent any ambiguity about potential artifacts induced by these anions[33,34]. Specifically, we resolved the structures of dolphin prestin reconstituted in lipid nanodiscs under three lipid conditions: thin lipids (PC14:1, resolution 3.5 Å), "mixed/regular lipids" (porcine brain lipid extract; resolution 2.9 Å), and thick lipids (PC20:1, resolution 3.0 Å) (**Fig. 1c; Extended Data Fig. 1-4; Supplementary Data Fig. 2**). Similar to the detergent condition reported previously[26], dolphin prestin (~ 80 kDa per monomer) is observed as a symmetric homodimer (C2 symmetry) composed of 14 α-helical transmembrane (TM) segments (**Extended Data Fig. 3**). The TM region is organized into two distinct domains that are a characteristic of SLC26 and other elevator-type transporters[35-43]: a gate domain, consisting of TM segments 5–7 and 12–14, and a core domain, which includes TM segments 1–4 and 8–11. The TM segment is domain-swapped with the cytoplasmic domain. Both N- and C-termini are positioned within the cytoplasmic regions (**Extended Data Fig. 3**).

Prestin protein reconstitution into extreme lipid environments, such as PC14:1 and PC20:1, was achieved using an "on-column" reconstitution method (see Methods), which enhances yield compared to conventional approaches[44,45]. The structures revealed distinct lipid-driven conformations. Under thin lipid conditions, prestin predominantly adopted an expanded "Sensor Down" state, characterized by the movement of the anion binding site towards the cytoplasm, and most notably, pronounced bending and tilting of the peripheral transmembrane helices 6 and 7 (TM6-7) (**Fig. 1d-f**). The bending motion of TM6-7 was further accompanied by more subtle movements in the gate domain, particularly in TM5b, to accommodate the hydrophobic mismatch (**Extended Data Fig. 4g).** Thick lipid and brain lipid environments stabilized a compact "Sensor Up" state. Notably, the brain lipid-bound structure resembled the Cl^--bound state observed in thick lipid nanodiscs, although the TM6-7 region exhibited structural instability and unresolved density in thick lipid conditions (**Fig1. c and Extended Fig. 4f**).

In all, the structural transitions observed in lipid bilayers with varying thickness suggest a crucial role of the gate domain, and especially the TM6-7 region as a mechanosensitive element, capable of bending and expanding to adapt to membrane deformation. Area changes of up to ~150 Å² across the membrane were observed (particularly in the inner leaflet), correlating with alterations in membrane thickness (**Fig. 1g**). Surprisingly, anion-binding interactions were preserved in all conditions, and a well-resolved Cl^- density was observed in both expanded and compact states (**Fig. 1f**). This contrasts with the absence of SO_4^{2-} density in detergent-solubilized conditions reported in previous studies[26,28].

Prestin responds to membrane stretch

In our previous study[26], using patch-clamp electrophysiology, we identified the critical role of TM6-7 in coupling voltage to motor movement in prestin. However, the mechanistic basis by which prestin senses membrane tension remains unclear. To correlate membrane thinning effects with tension, we conducted functional and structural experiments. Pressure-clamp electrophysiology was performed on native outer hair cells (OHCs) isolated from adult mice and on HEK293 cells overexpressing dolphin prestin, respectively. Controlled increases in intracellular pressure, which are expected to augment membrane tension, caused depolarizing shifts in the V_{pk} of NLC. Pressure-induced changes also enhanced linear capacitance in HEK293 cells, likely due to membrane swelling under applied tension. V_{pk} shifted from -75 ± 5 mV to -60 ± 5 mV in OHCs ($\Delta V_{pk}/\Delta P$: +6.9 ± 0.3 mV/mmHg, mean ± SEM, n=10) and from -57.3 ± 4.8 mV to -31.1 ± 11.1 mV in HEK293 cells (n = 6; mean ± SEM) (**Fig. 2a,b and Extended Data fig. 5a,b**). These findings confirm that prestin functions as an intrinsic mechanosensor, detecting and adapting to membrane tension in both native and heterologous systems.

To elucidate the structural basis of prestin's mechanosensitivity, we performed three-dimensional variability analysis of cryo-EM structures of prestin embedded in brain lipid nanodiscs (**Fig 2c, and Extended Fig. 2**). Notably, in addition to voltage sensor "elevator-like' movement (i.e., TMs 1,3, and 10), TM6-7 displayed the most pronounced conformational changes in prestin when transitioning from "Down-like" to "Up-like" conformations. Moreover, these transitions were accompanied by a striking deformation of the lipid nanodisc at prestin's periphery near TM6-7, emphasizing its role as a critical sensor (and effector) of the lipid bilayer environment.

We further employed hydrogen-deuterium exchange mass spectrometry (HDX-MS) to assess prestin's thermodynamic properties in different membrane environments (**Fig. 2d**; **Extended fig. 5c,d; Supplementary Data fig. 1**). Strikingly, residues in TM6 following the conserved Gly274 and Gly275 hinge exhibited heightened flexibility for nanodisc reconstituted prestin, as compared to detergent reconstituted prestin. Moreover, treatment of nanodisc-reconstituted prestin with α-cyclodextrin to extract phospholipids and induce tension augmentation/membrane thinning further increased the flexibility of the TM6 hinge region, linking its dynamic behavior to prestin's ability to sense and respond to lipids and mechanical forces. Collectively, these findings highlight prestin's inherent mechanosensitivity and the critical role of TM6-7 within the gate domain in sensing and adapting to changes in membrane tension and thickness. These changes are converted into charge transfer through an elevator-like movement of the core domain, which houses the putative voltage sensor (TM1, 3 and 10). We acknowledge that, while our findings demonstrate prestin's inherent mechanosensitivity, the cytoskeleton's potential role in tuning prestin's activity in situ under various conditions is plausible [46-48].

TM6-7 helix, "the electromotility elbow", is a key mechanosensing element in motor prestin

Single-point mutations in the conserved TM6-7 helical region of prestin result in distinct alterations to its voltage sensitivity. Specifically, the G274I mutation induces subtle hyperpolarizing shifts, while the G275I mutation causes depolarizing shifts[26] (**Extended fig. 6a**). These functional changes highlight the critical role of the TM6-7 region in prestin's electromotive cycle. To explore the structural basis of these functional changes, we generated the G274I and G275I mutants and determined their cryo-EM structures in detergent under Cl^--rich conditions at nominal resolutions of 2.9 Å and 3.4 Å, respectively (**Fig 2e-g and Supplementary Data Fig. 3**). The G274I mutant adopted a compact conformation, resembling the Sensor Up state, while the G275I mutant exhibited an expanded conformation, similar to the Sensor Down state.

Structural overlays revealed that the introduction of isoleucine at these positions altered the bending motion of the TM6-7 helix. In particular, while TM6 was straightened in the G274I mutant, the mutation at position 275 induced a kink located above its native position in wild-type (WT) prestin. This observation can be linked to the surrounding environment of the introduced mutations. The G274I mutation is facing the lipid bilayer and increases the stability of TM6 (**Fig. 2d**). This increased stability facilitates the formation of a "straightened" TM6 (and the associated compact state that favors a thick bilayer), thereby shifting the V_{pk} of this mutant towards hyperpolarized potentials. The G275I mutation, on the other hand, is pointing towards TM7, where in the compact conformation, G275 packs tightly against L292. In the G275I mutant, this packing is disrupted, and steric clashes between TM6 and TM7 increase the energy required for the formation of the straightened and compact TM6 (**Extended fig. 6b-c**), thereby shifting the V_{pk} of this mutant towards depolarized potentials[26]. Notably, evolutionary covariance analysis[49] revealed evolutionary coupling for amino acid at positions G275 and L292. This coupling is evident in prestin sequence alignments, where one residue typically has a bulky side chain while the other has a small or absent one. Consequently, the altered TM6 flexibility and bending/straightening propensity, as well as the disruption of TM6-TM7 interactions, are directly correlated with altered functional properties, linking these structural changes to functional outcomes.

The dynamic behavior of TM6-7 was further validated using hydrogen-deuterium exchange mass spectrometry (HDX-MS), which supported the observed conformational dynamics and confirmed the impact of the mutations on TM6-7 flexibility (**Fig. 2d**). Furthermore, intra-membrane area changes associated with the G274I and G275I mutants aligned with lipid-induced thinning experiments, highlighting the close coupling between prestin's structural states and lipid bilayer mechanics (**Fig. 2f**). Notably, despite these structural perturbations, the anion-binding site remained occupied in both the G274I and G275I mutants, consistent with the WT prestin structures in lipid nanodiscs (**Fig. 2g**). This finding suggests that while the mutations disrupt the flexibility of TM6-7 and alter prestin's conformational states, they do not directly affect the anion-binding site, highlighting the conserved role of this site in prestin's electromotive cycle. Therefore, the evolutionarily conserved G274 and G275 residues emerge as critical structural elements that facilitate prestin's conformational transitions, enabling the integration of mechanical and electrical signals for fast electromotility essential for mammalian cochlear amplification. This study unravels the structural dynamics of TM6-7 with prestin's ability to transduce mechanical signals, offering new insights into its molecular mechanism.

Anion interactions and their role in prestin's electromechanical coupling

Contrary to previous claims, our structures show that Cl^- remains bound to the anion-binding pocket in the "down" conformation of motor prestin, which is induced by the PC14 lipid environment and the G275I mutation, causing approximately 10% area expansion (**Fig. 1g, Fig 2f**). This observation supports the idea that a bound Cl^- works like a facilitator for gate-core interaction, and that introduction of a permanent negative charge (Asp or Glu) at the anion binding site (eg. S396D/E and S398D/E) renders prestin insensitive to changes in anionic conditions and S396D restores motor function to near WT levels, as previously proposed[27,29,50-52]. Whole-cell patch-clamp recordings in HEK293 cells expressing dolphin prestin revealed that the S396D mutant retained NLC with a V_{pk} of -72.5 ± 12.3 mV and slightly reduced voltage sensitivity (α) of 0.016 mV^{-1} (**Fig. 3 a,b**). Notably, the S396D mutant exhibited reduced sensitivity to salicylate, as the addition of 10 mM salicylate caused only a slight rightward shift in V_{pk} to -34.5 ± 6.4 mV, unlike the complete NLC abolition observed in the WT (**Fig. 3c**). These results confirm that the fixed negative charge introduced by aspartate can effectively mimic the role of Cl^- in stabilizing prestin's electromechanical cycle.

Structural analyses using cryo-EM revealed voltage Sensor Down and Up states of the S396D mutant embedded in detergent at nominal resolutions of 3.6 Å and 3.5 Å, respectively (**Fig. 3d-e**). The aspartate side chain was only resolved in the Sensor Up state, where it occupies a similar position to Cl^- in the WT anion-binding pocket. Particularly, the aspartate side chain is in close proximity to R399, thereby reducing the positive charge at the binding site. This reduction in positive charge may stabilize the binding site akin to Cl^- binding[26] and facilitates interactions between the hydrophobic surfaces of the core and gate domains (**Fig. 3g-h**). The voltage sensor up to down transition in the S396D mutant was accompanied by subtle outward tilting of the TM6-7 helices and intermediate membrane area expansion, linking the mutation to modified conformational dynamics (**Fig. 3e-f**).

To further explore whether charge neutralization alone drives these effects, we resolved the structure of WT dolphin prestin in nanodiscs composed of PC14:1 (thinner membrane) lipids in the presence of 10 mM salicylate at a nominal resolution of 3.7 Å (**Fig. 3i-k; Extended fig. 7)**. Interestingly, salicylate, a larger anion compared to Cl^-, outcompeted Cl^- in the thin lipid environment, locking the voltage sensor in an intermediate state similar to previously published structures in detergent[26,28] (**Fig. 3k; Extended fig. 7e,g**). The gate domain exhibited significant expansion, with TM6-7 helices displaying pronounced outward tilting and kinking, consistent with increased membrane area expansion (**Fig. 3j; Extended fig. 7d-f**). These observations are consistent with prior electrophysiological studies showing that larger anions reduce nonlinear NLC[22]. The salicylate ion is polar, with a significant negative charge concentrated around its carboxylate group, which binds directly to the positively charged anion binding

site. Meanwhile, the rest of the molecule, including the aromatic ring and phenol group, has hydrophobic properties that allow it to interact with the gate domain. This dual nature enables salicylate to latch onto both the core and gate domains of prestin. By doing so, it acts as a "glue", locking the entire assembly in place and preventing the sliding motions and tight packing of the individual domains that are crucial for prestin to couple electrical signals to mechanical motion. Together, the structural and functional data show that salicylate's size and polarity effectively immobilize the core and gate domains in WT prestin, disrupting its electromechanical coupling.

Unlike transporter SLC26A5, motor prestin has evolved to be inherently mechanosensitive

Most SLC26 members function as anion transporters[53]. Prestin is the only reported member of the SLC26 family of anion transporters with electromotive functional properties. Consistent with this evolutionary history, nonmammalian prestin orthologs mediate robust Cl^-/SO_4^{2-} exchange in heterologous systems. On the contrary, despite reports of active force generation mediated by prestin in chicken hair cells, there is currently no direct evidence for prestin-mediated somatic electromotility in hair cells from other nonmammalian vertebrates[54-56]. Moreover, electromotility has not been detected in heterologous systems for any nonmammalian prestin variants, hinting at intriguing functional and structural differences between orthologs[57-59]. We herein use lizard (*Anolis carolinensis*) SLC26A5, a closely related ortholog that has been reported to be non-electromotile in heterologous systems[59], as a model to examine the differences in the responses to membrane perturbations in prestin orthologs, and to investigate the evolutionary history of mechanosensitivity in prestin.

We first aimed to characterize the functional profile of lizard SLC26A5 in HEK293 cells. Notably, cells transfected with lizard SLC26A5 show clear electrogenic currents in the presence of extracellular SO_4^{2-} (**Fig. 4a**). Moreover, lizard SLC26A5 shows a broader NLC profile, with a shifted V_{pk} of 48.2 ± 4.1 mV at depolarizing potentials, and reduced voltage sensitivity (α) of 0.016 mV^{-1} (**Fig. 4b**). Similar to dolphin prestin, this NLC response is inhibited via extracellular application of 10 mM salicylate (**Extended fig. 8a**). Combined, this functional profile reflects lizard SLC26A5's primary role as an anion transporter rather than a motor protein.

Given that V_{pk} was already shifted toward positive potentials, we sought to test whether perturbing the lipid bilayer composition could shift it toward negative potentials, inspired by our findings with dolphin prestin. Attempts to modulate NLC in lizard SLC26A5 using thick lipids (ie PC20:1) induced transient shifts in V_{pk} towards negative potentials, whereas this V_{pk} returned to its original value within five to ten minutes (V_{pk} of 43.6 ± 3.7 mV) (**Fig. 4c,d, extended fig. 8b)**. Of note, this transient behavior was only observed for lizard SLC26A5, whereas the shift in V_{pk} was sustained for dolphin prestin. Moreover, we observed a sustained decrease in linear capacitance even after the V_{pk} returned to its original value, suggesting that the initial transient shift in V_{pk} is not solely due to changes in membrane thickness (**Extended fig. 8b**). Consequently, this highlights a fundamental difference in mechanosensory responses between motor prestin and a closely related transporter variant.

We further solved the structure of lizard SLC26A5 in a nanodiscs with brain lipid extract and PC20:1 (thick lipids) at nominal resolutions of 3.4Å and 3.6Å, respectively (**Fig. 4e-g, Extended fig. 8c-e**). Both conditions revealed a static, virtually identical inward-facing (Sensor Down) conformation with a Cl^- bound to the anion binding site. Moreover, TM6 adopts a straight conformation and lacks the dynamic TM6-7 reorientation observed in our inward-facing/expanded dolphin prestin structures (**Fig. 4g**). These findings suggest that mammalian motor prestin has evolved unique structural features, particularly in the TM6-7 region, enabling it to efficiently detect membrane deformation and couple mechanical forces to electrical signals.

Molecular principles of electromechanical coupling in motor prestin

Prestin, a piezoelectric motor protein in OHCs, mediates somatic electromotility by converting electrical signals into mechanical motion and vice versa. This process is pivotal for sound amplification within the cochlea, especially at high frequencies where OHC-driven electromotility enhances basilar membrane vibrations. The efficiency of this amplification is contingent upon the rapid, precise response of prestin, which operates within the electrical constraints set by the RC time constant of the cell[60-62]. Recent advanced measurements in vivo and in vitro have extended prestin's functionality due to voltage stimulation to frequencies approaching 19-20 kHz[63,64]. At ultrasonic frequencies (>20 kHz), prestin may also contribute to basilar membrane vibrations either passively by modulating the system's mechanical properties[65] and/or actively by altering local gating charges in response to mechanical forces[66]. Here, we present high-resolution insights into how prestin detects membrane tension or deformation and translates it into charge transfer, highlighting its role in mechanotransduction at the molecular level. The sensitivity of prestin to membrane tension/thickness may be crucial for the cooperative action of prestin to maximize electromotility output.

Specifically, our study unequivocally shows that motor prestin responds to membrane thinning and membrane tension, similar to other membrane-tension gated mechanosensitive channels like MscL, MscS, and Piezo1. Upon membrane thinning, prestin transitions from a compact to an expanded conformation (up to 10% change in the area motor), shifting the voltage sensor from the "Up" to the "Down" state. This change links mechanical force to charge movement across the membrane, shedding light on how OHC electromotility affects charge dynamics at high frequencies. In contrast, lizard SLC26A5, a robust transporter, shows distinct mechanosensory properties. When large anions occupy the binding site, both motor and transporter prestin activities are inhibited, supporting the idea that anion occlusion regulates prestin's function. A molecular model (**Fig. 4h**) illustrates how prestin's mechanosensitivity may act as mechanical gain for tuning electromotility. This evolutionary refinement highlights prestin's structural and functional plasticity, essential for OHC motility and cochlear amplification.

In summary, our results demonstrate that Cl^- is not merely a passive participant but an integral part of prestin's voltage-sensing mechanism. The ability of a fixed negative charge, as seen in the S396D mutant, to substitute for Cl^- highlights the critical role of charge neutralization in prestin function. Furthermore, lipid environment and steric effects of anion binding emerge as key modulators of prestin's conformational dynamics, providing valuable insights into its electromechanical cycle. This molecular model demonstrates how motor prestin senses membrane forces through lipid interactions, explaining its dual role as both a motor protein and a mechanosensitive motor.

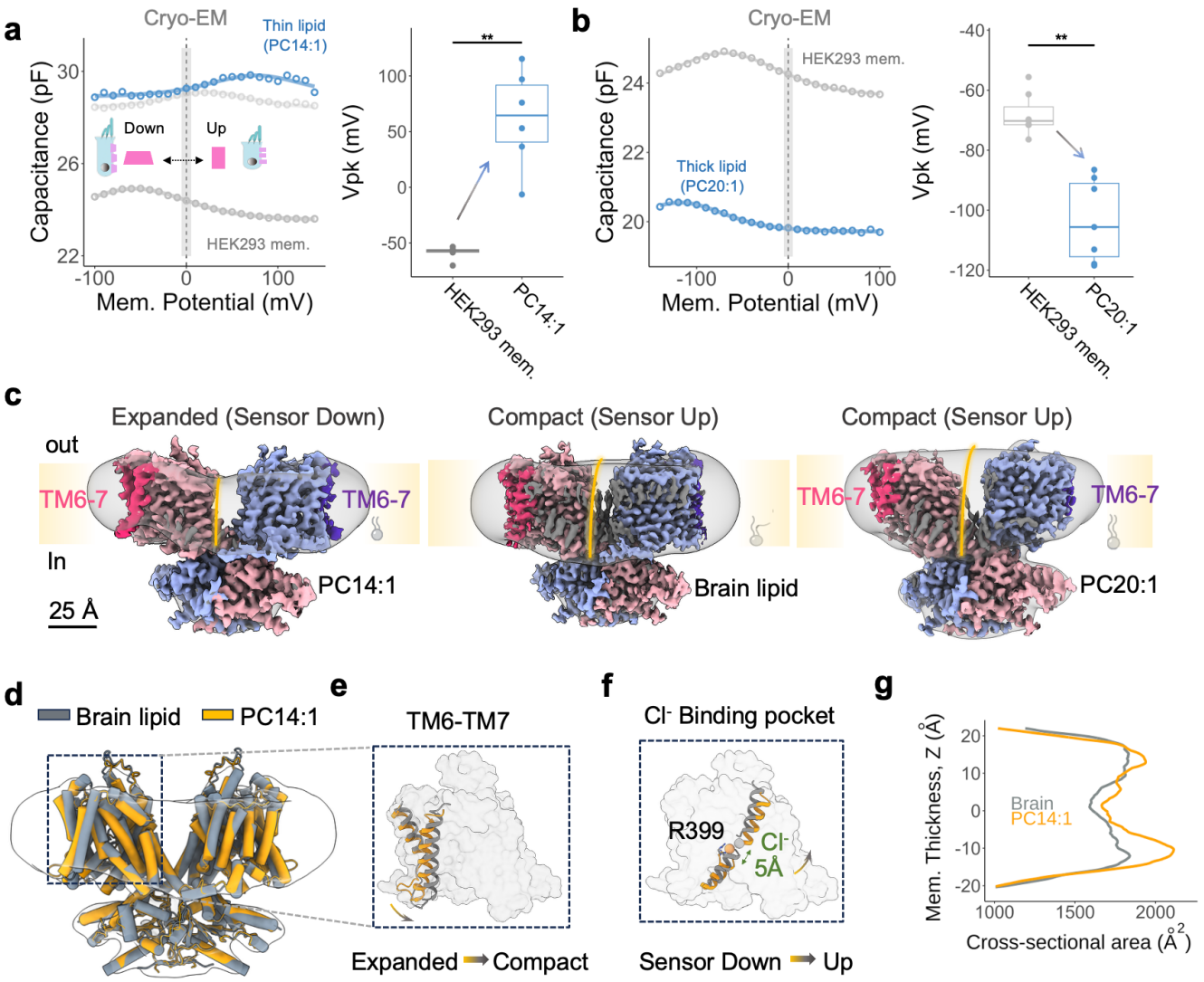

Fig. 1: Lipid-mediated conformational changes in motor prestin from expanded (Sensor Down) to compact (Sensor Up) states. a) Whole-cell patch-clamp electrophysiology was performed on HEK293 cells transfected with wild-type dolphin prestin using physiological solutions (see Methods). Nonlinear capacitance (NLC) was recorded before and after the addition of 1 mM α-cyclodextrin doped with PC14:1 (thin) lipid, mimicking membrane thinning during somatic elongation. Lipid delivery shifted the V_{pk} of NLC from -58.7 ± 3.0 mV to depolarized potentials (+61.9 ± 21.0 mV, mean ± SEM), accompanied by an increase in linear capacitance, likely due to reduced membrane thickness. **b)** To simulate outer hair cell contraction, α-cyclodextrin was doped with PC20:1 (thick) lipid and delivered to the plasma membrane. This caused a hyperpolarizing shift of V_{pk} from -57.8 ± 3.0 mV to -93.6 ± 4.2 mV and a decrease in linear capacitance, consistent with membrane thickening. Together, these results demonstrate that membrane thickness modulates charge transfer in prestin, transitioning between the expanded (Sensor Down) and compact (Sensor Up) states (n = 6; mean ± SEM). **c)** Cryo-EM density maps and the overall structure of the dolphin prestin homodimer were solved in MSP1-E3D1 nanodiscs under three lipid conditions: PC14:1 (left, Expanded [Sensor Down] state), brain lipid extract (middle, compact [Sensor Up] state), and PC20:1 (right, compact [Sensor Up] state). The nominal resolutions of

the structures are 3.0 Å, 2.9 Å, and 3.5 Å, respectively. Scale bar = 25 Å. Yellow lines indicate nanodisc thickness. Monomers are shown in blue and salmon. The TM6-7 region is highlighted in dark pink and dark violet. Note that the TM6-7 region in the PC20:1 structure is not fully resolved, while the TM6-7 helices in the PC14:1 lipid (thin lipid) exhibit slight tilting. **d)** Structural overlay of prestin in the compact (Sensor Up) and expanded (Sensor Down) states, depicted as cartoon models. **e)** Transmembrane helices TM6-TM7 undergo significant conformational changes, bending at the gating region to accommodate varying bilayer thickness. **f)** Anion density, previously identified as Cl^-, was observed within the binding site in both the compact and expanded states, suggesting its role in the electromotive cycle. As the voltage sensor undergoes an elevator-like motion, Cl^- elevates down ~5 Å from the Sensor Down (expanded) to the Sensor Up (compact) conformation. **g)** Membrane thinning caused an expansion in the motor domain area of prestin (transmembrane domain). Residues 460 to 505 were used for dimer alignment, and cross-sectional area changes were calculated for a single monomer.

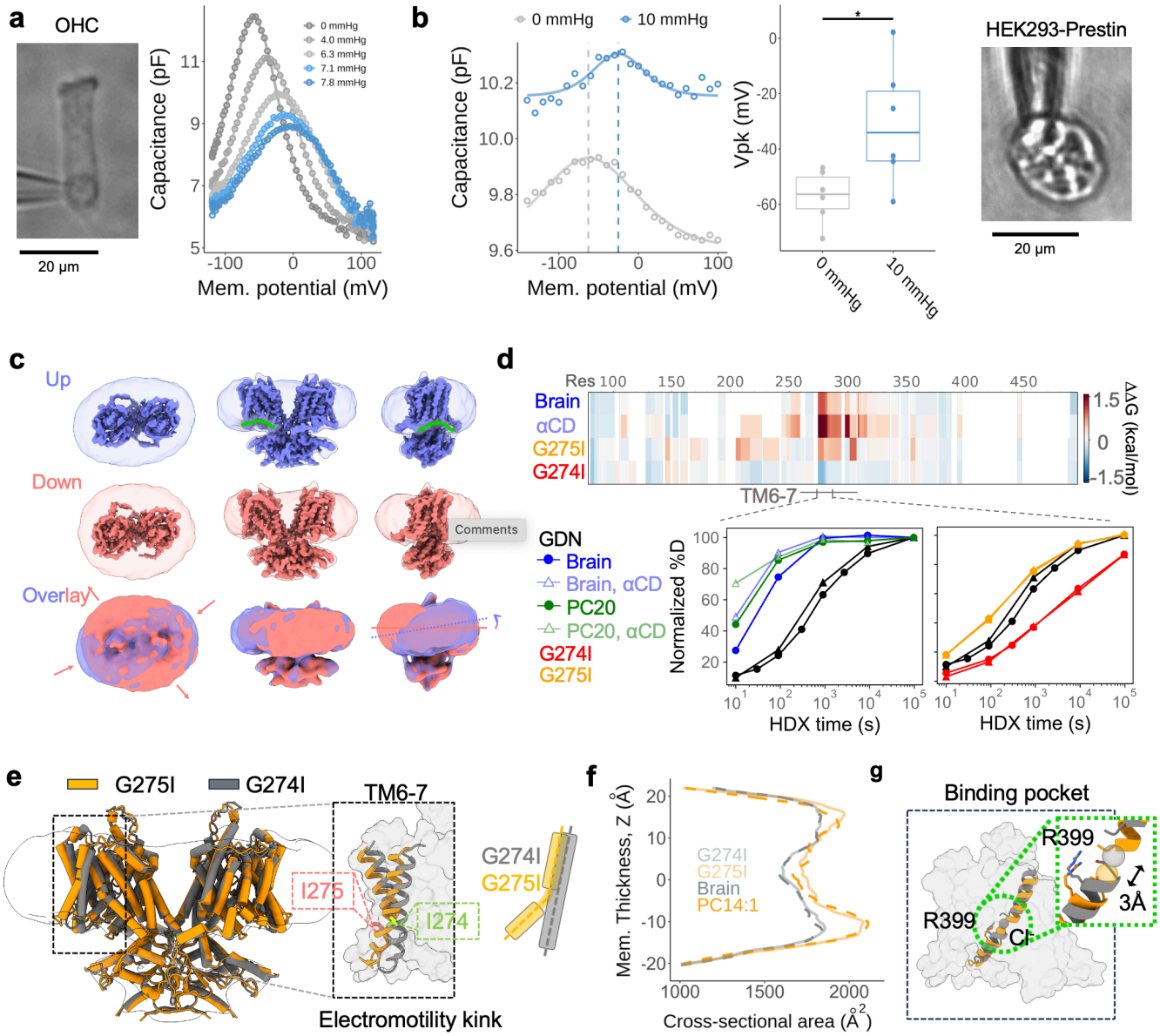

Fig. 2: Inherent mechanosensitivity of motor prestin and the role of the evolutionarily conserved flexible region in the TM6-7 gating domain in sensing membrane-mediated mechanical forces. a) Whole-cell patch-clamp electrophysiology was performed on outer hair cells isolated from adult (P21) mice and on **b)** HEK293 cells overexpressing dolphin prestin. They were both subjected to controlled intracellular pressure using a high-speed pressure clamp to induce plasma membrane tension. This approach mimicked outer hair cell elongation and shrinkage, enabling simultaneous monitoring of prestin's charge transfer and changes in nonlinear capacitance (NLC). In both cell types, the NLC exhibited depolarizing shifts with increasing tension: the V_{pk} shifted from -75 ± 5 mV to -60 ± 5 mV in outer hair cells (n = 10; mean ± SEM) and from -57.3 ± 4.8 mV to -31.1 ± 11.1 mV in HEK293 cells (n = 6; mean ± SEM). Linear capacitance increased in most cases, likely due to membrane swelling. These results demonstrate the mechanosensitivity of prestin's charge transfer in both native and heterologous systems. **c)** 3D variability analysis of prestin in brain lipid nanodiscs revealed expanded and compact states associated with severe membrane deformation, including thinning and changes in local curvature. **d)** Hydrogen-deuterium exchange mass spectrometry (HDX-MS) revealed that the TM6-7 region (particularly after the double Gly274-Gly275 residues), which is lipid-facing, showed the most

pronounced thermodynamic changes in response to alterations in the lipid environment. This was confirmed using various conditions, including reconstitution of prestin into nanodiscs with brain lipid extract or thick (PC20:1) lipids, and lipid extraction from these nanodiscs via α-cyclodextrin. The G274 and G275 residues are evolutionarily conserved, and mutations in this region severely impact charge transfer. Notably, HDX-MS reveals similar changes in the TM6-7 region for G274I and G275I mutants (purified in Gdn) as compared to membrane perturbation, highlighting the role of this region in sensing lipid bilayer properties. **e)** Structure overlay of prestin mutants G274I and G275I were solved under Cl^- conditions in detergent, solved at nominal resolutions of 2.9A and 3.4A respectively. The G274I mutant exhibited the most compact state, while G275I showed the most expanded state. Structural overlays revealed that the kink in TM6 caused by G275I shifted to a glycine residue above its wild-type position, likely due to the increased bulkiness of the isoleucine substitutions, which restricted full straightening of the TM6-7 region. These structural changes correlated with hyperpolarizing (G274I) and depolarizing (G275I) voltage sensitivity shifts. **f)** Membrane area changes associated with these mutations mirrored those observed during membrane thinning, reinforcing the functional connection between prestin's TM6-7 region and lipid bilayer mechanics. **g)** The anion-binding site, previously identified as Cl^-, remained occupied in both mutants, consistent with lipid nanodisc structures, further supporting the anion's conserved role in the electromotive cycle.

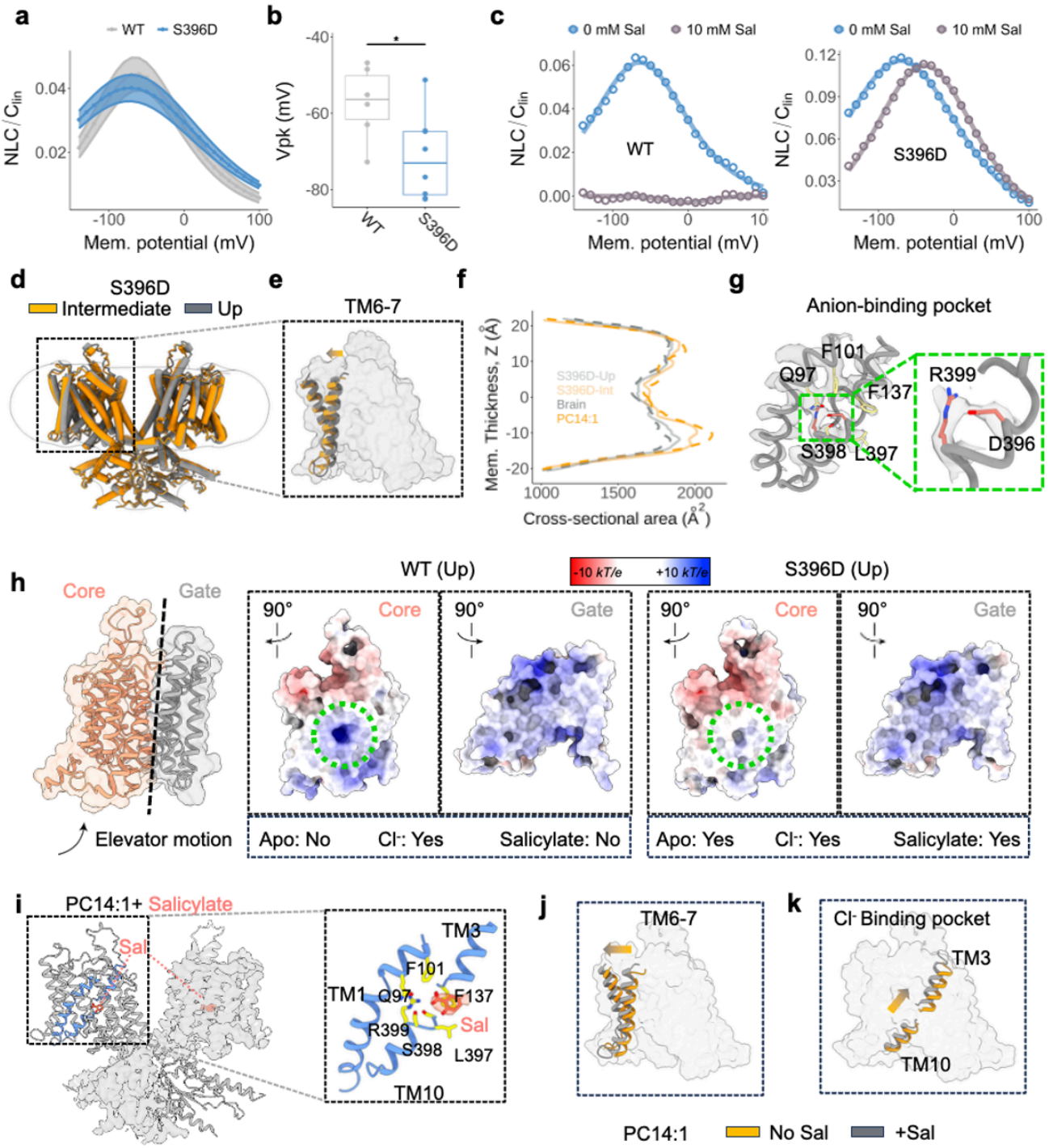

Fig. 3: Structural visualization of the role of anions in motor prestin function and electromechanical coupling. a) Whole-cell patch-clamp electrophysiology in HEK293 cells, overexpressing dolphin prestin, demonstrates that replacing a serine with a negatively charged residue, Asp (S396D), in the anion-binding pocket restores motor function to near wild-type levels. **b)** Functionally, the S396D mutant exhibits a V_{pk} of -72.5 ± 12.3 mV and slightly reduced voltage sensitivity (α) of 0.016 mV^{-1}. (n = 6; mean ± SEM) **c)** Unlike wild-type Prestin, where NLC is completely abolished after the addition of 10 mM salicylate, the S396D mutant shows only a slight rightward shift to -34.5 ± 6.4 mV, indicating reduced sensitivity to salicylate mediated inhibition. (n = 5; mean ± SEM) **d)** High-

resolution cryo-EM structures of the S396D mutant were solved in Gdn at a nominal resolution of 3.5 Å and 3.7 Å, revealing both intermediate and Sensor Up states. **e**) Despite the single-point mutation in the anion binding site (voltage sensor), the TM6-7 domain displays slight outward titling, **f**) with intermediate expansion levels noted in membrane area changes. **g)** In the "up" state, the density of the S396D side chain occupies a position analogous to where Cl^- is observed in the wild-type anion-binding site. This demonstrates that a permanent charge, such as D, can functionally replace Cl^- at this critical site. **h)** The mechanism by which a negatively charged residue replaces Cl^- involves modulation of the interfacial charge distribution between the core domain and the gate domain. In the absence of an anion, the anion-binding site remains positively charged, while the gate domain interface (the mechanosensory region) is neutralized. For allosteric interaction between these domains to occur, the hydrophobic surfaces must slide against each other, facilitated by the presence of either an anion (wild-type) or a charged residue such as D (S396D). This surface interaction allows mechanical force sensed by the gate domain to be transmitted to the core domain and vice versa. **i**) The structure of dolphin prestin embedded in nanodiscs composed of PC14:1 (thin membrane) lipids in the presence of 10 mM salicylate was resolved at nominal resolution of 3.7 Å. **j)** In PC14:1 (thin membrane), the gate domain is expanded, but (**k**) the voltage sensor is locked in an intermediate state. TM6-7 are tilted and kinked outward, leading to area expansion in the gate domain.

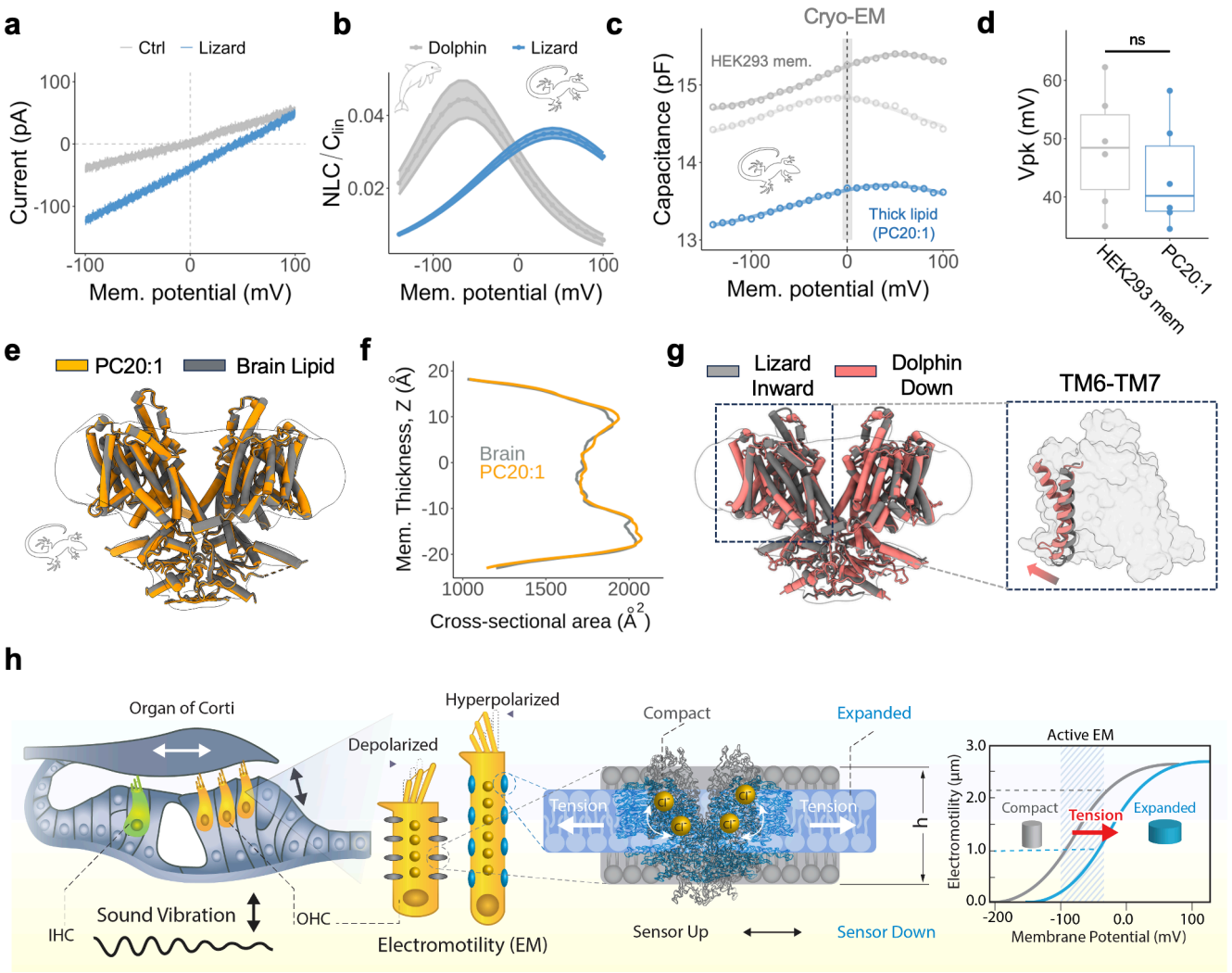

Fig. 4: Evolutionary adaptations of motor Prestin for sensing membrane-mediated mechanosensitivity: Structural and functional distinctions between transporter SLC26A5 and motor Prestin. a) Lizard SLC26A5 displays robust Cl^-/SO_4^{2-} exchange activity, and (**b**) exhibits reduced nonlinear capacitance (NLC) compared to motor Prestin, functioning primarily as an anion transporter. In HEK293 cells overexpressing Lizard SLC26A5, the NLC V_{pk} is observed at depolarizing potentials, and voltage sensitivity is reduced (V_{pk} = 42.2 ± 6.4 mV, α = 0.016 mV^{-1}, n = 6 ± SEM). **c,d)** Modulation of NLC with PC20:1 lipids initially induces a leftward shift (indicated by traces in light grey) but, unlike motor Prestin, later reverts to the original V_{pk}, highlighting a mechanosensory response distinct from that of motor Prestin. (n = 6) **e)** Overlay between the lizard SLC26A5 structures determined in brain lipid extract and PC20:1 nanodiscs. Despite changes in membrane thickness, lizard SLC26A5 consistently adopts a homodimeric, downward-facing conformation without TM6-7 rearrangements, distinct from the structural dynamics observed in motor Prestin. This structural rigidity suggests lizard SLC26A5 lacks the evolutionary adaptations required for mechanosensitivity. **f)** Consistent with the absence of clear conformational differences, the structures of lizard SLC26A5 in brain lipid extract and PC20:1 occupy a nearly identical intra-membrane cross-sectional area. **g)** Structural overlay of dolphin prestin in the expanded (Sensor Down) state and lizard prestin in the downward-facing state reveals key differences in the TM6-7 region of the gate domain, but minimal rearrangements involving the anion binding site. **h)** Our molecular model suggests motor prestin's mechanosensitivity allows it to finely tune its electromotility in response to membrane-mediated mechanical forces. As membrane stretch shifts prestin from a compact (Sensor Up) to an expanded (Sensor Down) conformation, gate/core electromechanical coupling provides an adaptive gain control mechanism. This dynamic

regulation could prevent saturation at high sound intensities while simultaneously boosting amplification at lower intensities, optimizing sound perception.

Acknowledgments: Acknowledgments

We thank Drs Omid Bavi, Charles Cox, Boris Martinac, Zijin Zhou, Pancho Bezanilla, and members of the Perozo and Bavi labs for a healthy exchange of ideas and comments on the manuscript. We are grateful to Dr. Peng Shi for sharing the Tursiops Prestin plasmid and David He for the Lizard SLC26A5 construct. We also thank James Fuller, Joe Austin II, and Tera Lavoie at the University of Chicago Advanced Electron Microscopy Facility for microscope maintenance and training. This work was supported by NIDCD grant R01 DC019833 (to E.P.) and NIH/NIDCD DC017482 (to K.H.). This research was in part supported by the National Cancer Institute's National Cryo-EM Facility at the Frederick National Laboratory for Cancer Research under contract HSSN261200800001E.

Author contributions: N.B. and E.P. conceived the project, provided reagents, and with P.H. wrote the manuscript with input from all other authors. N.B. and P.H. expressed and purified the protein, prepared cryo-EM grids, processed the cryo-EM data, built and refined the atomic models, managed cell culture, and, along with K.H., performed and analyzed the electrophysiological experiments. N.B. and P.H. also carried out molecular cloning, mutagenesis, and created all expression constructs with W.M.. N.B., P.H., and M.Z. performed EM data collection. X.L. and T.S. performed and analyzed the HDX-MS. All authors analyzed the data.

Competing interests: Authors declare no competing interests.

Materials and Methods

Cell lines

The cell lines used in this study are similar to the ones used previously. Suspension HEK293S GnTI$^-$ cells were obtained from ATCC (ATCC CRL-3022) and used for large-scale expression of dolphin and lizard prestin. These cells were grown at 37°C and 7.8% CO_2 in FreeStyle™ 293 expression medium (Gibco Fisher Scientific) supplemented with 10 µg/ml penicillin/streptomycin (Company) and 2% heat-inactivated fetal bovine serum (FBS) (Company). Adherent HEK293T cells were obtained from ATCC (ATCC CRL-3216) and used for patch-clamp electrophysiology experiments. They were cultured at 37°C and 5% CO_2 in in Dulbecco's Modified Eagle's Media (DMEM, Gibco Fisher Scientific) supplemented with 10% heat-inactivated FBS. Suspension Sf9 insect cells (Thermo Fisher, 12659017) were used for baculovirus production. They were grown at 28 °C in SF-900 II SFM (Thermo Fisher, 10902096) medium supplemented with 10% heat-inactivated FBS and 10 µg/ml Gentamicin (Company).

Generation of prestin constructs

The cloning strategy for dolphin prestin was described previously[26]. A similar strategy was used for lizard prestin, which was a generous gift from the Shi lab[31]. Briefly, the DNA sequence encoding dolphin or lizard prestin was subcloned into a pEG BacMam vector with a C-terminal HRV-3C protease site, an eGFP, and an 8x-His tag using restriction digestion. This construct was used for P0 baculovirus production using Cellfectin II (Thermo Fisher, 10362100) and the Bac-to-Bac (invitrogen) method. P0 baculovirus was amplified once to generate P1 virus. The coding sequences for prestin genes were further subcloned into a pEG BacMam vector lacking C-terminal tags. This construct was used for electrophysiological experiments. A construct encoding eGFP alone was generated by subcloning the eGFP coding sequence into a pcDNA3.1 vector using restriction digestion. This construct was used as a transfection marker for electrophysiological experiments. The G274I, G275I, and S396D mutations were introduced into the dolphin prestin constructs using KOD DNA polymerase (EMD Millipore, 71085), and the QuikChange site-directed mutagenesis (Agilent) method. The sequence of each plasmid construct was confirmed by DNA sequencing prior to use.

Protein expression

The same strategy as previously described[6] was used for large-scale protein expression and purification of dolphin and lizard prestin. HEK293S GnTI- cells were grown at 37 °C until reaching a confluency of 2.4 to 2.8 million cells/ml. At this confluency, cells were infected with 1:10 v/v P1 baculovirus. After 12-24 hours at 37 °C, the cells were supplemented with 10 mM sodium butyrate and transferred to 30 °C for another 36 to 48 hours (until 60 hours post infection). At this point, the cells were harvested via low-speed centrifugation at 6,000 rpm and 4 °C for 20 minutes, resuspended in phosphate-buffered saline (PBS) at pH 7.4, and spun down again. The resulting pellet was flash frozen in liquid nitrogen and stored at -80 °C until further processing.

Protein purification and "on-column" nanodisc reconstitution

The same purification protocol was used for dolphin and lizard prestin, and a Cl^- based buffer was used as the base solution for all purification steps. This buffer consisted of 150 mM NaCl, 20 mM Tris-HCl, 1 mM EDTA, and 3 mM DTT at pH 7.5, and is referred to as Buffer A. To start the purification, the pellets were thawed in a water bath at room temperature, resuspended in Buffer A supplemented with a tablet of cOmplete™ Protease Inhibitor Cocktail (Roche), 1 µg/ml Aprotinin, 1 µg/ml Leupeptin, 1 µg/ml Pepstatin, 0.2 mM PMSF, and 10 µg/ml DNase. All subsequent steps were performed at 4 °C. After

resuspension, the cells were dounce homogenized, and 1% n-dodecyl-β-D-maltopyranoside (DDM; Anatrace) and 0.2% cholesteryl hemisuccinate (CHS, Anatrace) was added for protein extraction while rotating for 90 minutes. The cellular debris was separated via ultracentrifugation at 40,000 rpm for 45 minutes, and the supernatant containing the solubilized protein was collected and mixed with GFP-nanobody coupled CNBR-activated Sepharose beads (GE healthcare) for 90 minutes. The GFP-nanobody coupled resin was prepared as previously described[26,67]. After binding, the resin was collected and washed in Buffer A with different detergent compositions: the first wash buffer was supplemented with 0.05% DDM and 0.01% CHS; the second was supplemented with 0.05% DDM, 0.01% CHS, and 0.02% glyco-diosgenin (GDN; Anatrace); the third was supplemented with 0.02% GDN. After the third wash step, the protein was either cleaved with HRV-3C protease[68] for 2-4 hours (for detergent-based samples) or subjected to a modified on-column nanodisc reconstitution[69].

Three different lipid compositions were used for nanodisc reconstitution. "Brain lipid" consisted of pure porcine brain lipid extract (Avanti Polar Lipids); "Thin lipids" consisted of 90% PC14:1 (Avanti Polar Lipids) and 10% brain lipid extract; "Thick lipids" consisted of 90% PC20:1 (Avanti Polar Lipids) and 10% brain lipid extract. In all cases, lipids solubilized in chloroform were first dried using rotary evaporation, resuspended in Buffer A, and solubilized using a final concentration of 3% GDN, sonication, and freeze-thaw cycles until the solution was completely transparent. The solubilized lipids were either used immediately, or stored at -80 °C. For all nanodisc samples, MSP1-E3D1 was used as the belt protein and prepared as previously described (Alvarez et al, 2010). A prestin dimer to MSP to lipid ratio of 1:5:500 was used in all cases. Given that we could not measure the exact concentration of prestin bound to resin, the yield was estimated based on previous experience and multiplied by two to ensure addition of sufficient lipids and MSP. To initiate the reconstitution, lipids were added to the protein bound resin, incubated for 5 minutes, and then purified MSP was added. After 20 minutes of incubation, detergent was removed overnight via three successive rounds of Biobeads (Bio-Rad) addition. The next day, the nanodisc reconstituted protein bound to the resin was washed with 50 ml Buffer A containing no detergent, and subsequently cleaved with HRV-3C protease for 2-4 hours.
Both detergent and nanodisc samples were eluted post HRV-3C cleavage and concentrated using a 100 kDa MW cutoff centrifugal filter (Millipore concentrator unit) for size-exclusion chromatography (SEC) using a Superose 6, 10/300 GE column (GE Healthcare). The running buffer for detergent samples consisted of Buffer A supplemented with 0.02% GDN, 1 μg/ml Aprotinin and 1 μg/ml Pepstatin, whereas the running buffer for nanodisc samples consisted of Buffer A supplemented with 1 μg/ml Aprotinin and 1 μg/ml Pepstatin. Peak fractions were concentrated to 2-3 mg/ml using a 100 kDa MW cutoff centrifugal filter and immediately used for cryo-EM grid preparation. For the PC14-Salicylate sample, Na-Salicylate was further added to the concentrated sample at a final concentration of 10 mM prior to grid freezing.

Cryo-EM sample preparation and data collection

The dolphin prestin brain lipid nanodisc sample was frozen onto Quantifoil 200-mesh 1.2/1.3 Copper grids (Quantifoil), whereas UltrAuFoil 300-mesh 1.2/1.3 Gold grids (Quantifoil) were used for all other samples. In all cases, the grids were glow-discharged at 20W for 30-45s using a Solarus Plasma Cleaner (Gatan). A 3.5 μl volume of purified prestin protein was then applied onto each glow-discharged grid and subsequently plunge-frozen into liquid nitrogen cooled liquid ethane using a Vitrobot Mark IV (Thermo Fisher) at 100% humidity and 22°C with a blot time of 3-5s and blot force 1.

The data for the dolphin prestin G275I mutant and dolphin prestin PC14 nanodisc with salicylate was collected at the National Cryo-Electron Microscopy Facility at the National Cancer Institute (NCI) on a Titan Krios (Thermo Fisher) equipped with a K3 camera and GIF energy filter (Gatan) at 81,000x magnification, resulting in a physical pixel size of 1.12Å. Movies were collected using a total dose of

50 e^{-} $Å^{-2}$ divided into 50 fractions. The movies for the remaining samples were collected at the University of Chicago Advanced Electron Microscopy Facility on Titan Krios G3 (Thermo Fisher) equipped with a K3 camera and GIF energy filter (Gatan) at 81,000x magnification, corresponding to a 1.068Å physical pixel size. The data was acquired using a total dose of 60 e^{-} $Å^{-2}$ divided into 52 frames. The data collection statistics are summarized in table 1.

Cryo-EM data analysis

All of the cryo-EM data was analyzed using a combination of Relion[1,2 70,71] and cryoSPARC[72], and a similar processing strategy was used for all samples. The raw movies were first subjected to beam-induced motion correction using Relion, and the resulting micrographs were transferred to cryoSPARC for patch-based CTF estimation, micrograph curation, and blob particle picking. The particles were extracted using a box size of 256 Fourier cropped to 128 and subjected to one round of 2D-classification to generate templates for template-based particle picking. These particles were again extracted with a box size of 256 Fourier cropped to 128 for several rounds of 2D-classification. Classes that showed prestin-like features were re-extracted without Fourier cropping to generate multiple ab-initio models using C1 symmetry. In all cases, the ab-initio reconstruction job yielded a single good class and additional "junk" classes, which were used as inputs for subsequent rounds of heterogeneous refinement with C1 symmetry. The particles and map corresponding to the best class were then subjected to local CTF and Non-Uniform refinement[73] with either C1 or C2 symmetry applied. No clear differences were observed for any of the samples, and thus, the C2 symmetric reconstruction was used for downstream processing. For all dolphin prestin datasets, the particles were transferred back to Relion for Bayesian Polishing[5]. For the lizard SLC26A5 datasets, the particles were subjected to reference-based motion correction in cryoSPARC instead. In all cases, the polished/motion-corrected particles were used for an additional round of CTF and Non-Uniform refinement in cryoSPARC. Local resolution estimation and 3D variability analysis were performed in cryoSPARC. Sample processing workflows can be found in Extended Data Figs. 1 and 2, and in Supplementary Data Figure 5. The Relion software used to process cryoEM data was curated by SBGrid.

Model building and molecular visualization

The models reported in our previous publication[26] corresponding to the "Up" (PDB ID: 7S8X) and "Down I" (PDB ID: 7S9B) conformations were used as initial templates for the dolphin prestin models in this manuscript. In the case of lizard SLC26A5, ColabFold[74] was used to generate an initial template. The predicted structure was first rigid-body fit to the map of lizard SLC26A5 in brain lipid nanodiscs, and residues that lacked clear density were removed manually. The corresponding regions include the N-terminus (residues 1-13), C-terminus (residues 728-739), and IVS (residues 587-641). In all cases, the initial template was first subjected to one round of real-space refinement in Phenix[75] with morphing and simulated annealing enabled. The outputs from this job were then manually inspected and iteratively refined using a combination of Phenix real-space refinement, Coot[76], and Isolde[77]. Residues with poor side chain density were modeled as alanines. The surface electrostatics for the core and gate domains were calculated using the PBEQ solver[78] in CHARMM-GUI[79]. UCSF ChimeraX[80] was used for molecular visualization and analyses. The evolutionary coupling analysis was performed using the EVcouplings web-server[49].

Patch-clamp electrophysiology in HEK293 cells

Adherent HEK293T cells were used for all heterologous expression experiments. The cells were plated 24 hours before transient transfection. For each transfection, 2.5–3 µg of prestin plasmids and 0.4 µg of

eGFP plasmid were mixed with 8 µl of Lipofectamine® 3000 (ThermoFisher Scientific) at a reagent-to-DNA ratio of 2:1 in 125 µl of Opti-MEM (Life Technologies). After 20–24 hours of incubation at 37 °C, the cells were transferred to 30 °C to enhance protein expression. Successfully transfected cells were used for nonlinear capacitance (NLC) measurements after 24–48 hours.

For NLC measurements, we followed the same method described previously[26]. Briefly, membrane capacitance was measured in the whole-cell configuration using a 1 kHz sine wave stimulus with a 10 mV amplitude, applied during voltage steps 10 ms after the transient response. Voltage steps ranged from -120 mV to +100 mV, with a holding potential of -70 mV. The admittance (Y(ω)) of the system was determined by spectral analysis, and the DC conductance (g) was derived from the steady-state current preceding the sine wave stimulus. The circuit components, capacitance (C), membrane resistance (Rm), and series resistance (Rs), were calculated accordingly[81] and explained in details previously[26]. For the positive pressure experiments (to create membrane tension) in HEK293 cells, cells overexpressing dolphin prestin were subjected to positive pressure of either 0 or 10 mmHg using a High-Speed Pressure Clamp-1 apparatus (ALA Scientific Instruments, Farmingdale, NY, USA), while simultaneously measuring NLC in whole-cell mode.

For all the experiments done for motor (dolphin) prestin, the internal solution typically contains 130 mM CsCl, 2 mM $MgCl_2$, 10 mM EGTA, 10 mM HEPES, and 5 mM Na_2ATP, with the pH adjusted to 7.2-7.4 using CsOH and osmolarity set to 290-300 mOsm, supplemented with sucrose if necessary. The external solution typically contains 140 mM NaCl, 5 mM KCl (or less if minimizing potassium currents), 2 mM $CaCl_2$, 1-2 mM $MgCl_2$, 10 mM HEPES, and 10 mM glucose, with the pH adjusted to 7.2-7.4 using NaOH and the osmolarity set to ~300-310 mOsm, supplemented with sucrose if required. Identical solutions were used for NLC measurements involving lizard SLC26A5. For electrogenic Cl^-/SO_4^{2-} antiport measurements of transporter (Lizard) SLC26A5, the solutions were almost identical to the ones described previously.[43] Briefly, the internal solution contained 10 mM CsCl, 10 mM Cs_2SO_4, 130 mM potassium L-aspartate, 2 mM $MgCl_2$, 10 mM EGTA, and 10 mM HEPES. The pH was adjusted to 7.4 using CsOH. The external solution typically contained 120 mM NaCl, 20 mM TEA-Cl, 2 mM $CoCl_2$, 2 mM $MgCl_2$, and 10 mM HEPES. The pH was adjusted to 7.4 using NaOH. Command voltage ramps from -100 mV to +100 mV or -130 mV to +130 mV were used to measure electrogenic transport currents. Data for all electrophysiological experiments comes from three independent rounds of transfection.

Modulation of bilayer thickness

Membrane thickness modulation was achieved by incubation of cells with α-cyclodextrin-PC14:1 (thin lipids) or α-cyclodextrin-PC20:1 (thick lipids) complexes. To generate the complexes, 10 mg of PC14:1 or PC20:1 (Avanti Polar Lipids) dissolved in chloroform was dried using rotary evaporation. The dried lipid film was resuspended in 1 ml of external blocking solution supplemented with 20 mM α-cyclodextrin (Sigma-Aldrich) through bath sonication, generating a stock solution with approximately a 2:1 α-cyclodextrin to phospholipid molar ratio. Of note, complete lipid solubilization was not achieved at this high lipid concentration, and a small amount of precipitate remained despite extensive bath sonication. During recordings, the NLC was first measured prior to modulation of bilayer thickness. Subsequently, external blocking solution with the α-cyclodextrin-PC14:1 or α-cyclodextrin-PC20:1 complex was added to the experimental chamber to reach a final concentration of ~1 mM α-cyclodextrin in the bath solution, and NLC was measured over several minutes until the giga seal was lost (up to 15 minutes).

Animals

Wild-type FVB/NJ mice (3-7 months of age) were used to obtain OHCs. The euthanasia procedure was approved by Northwestern University's Institutional Animal Care and Use Committee.

NLC recording in OHCs

OHCs were isolated as described previously[82]. Whole-cell recordings were performed at room temperature using the Axopatch 200B amplifier (Molecular Devices) with a 10 kHz low-pass filter. Recording pipettes pulled from borosilicate glass were filled with a solution containing (mM): 140 CsCl, 2 $MgCl_2$, 10 EGTA, and 10 HEPES (pH 7.4). Cells were bathed in an extracellular solution containing (mM): 120 NaCl, 20 TEA-Cl, 2 $CoCl_2$, 2 $MgCl_2$, 10 HEPES (pH 7.4). Osmolality was adjusted to 309 mOsmol/kg with glucose. The intracellular pressure was controlled manually and monitored by a pressure manometer (PM01D, WPI). The electric current response to a sinusoidal voltage stimulus (2.5 Hz, 120 mV amplitude) superimposed with two higher frequency stimuli (390.6 and 781.2 Hz, 10 mV amplitude) was recorded by jClamp (SciSoft Company). C_m was determined by a fast Fourier transform-based admittance analysis[5].

NLC data analysis

Voltage-dependent C_m data were analyzed using the following two-state Boltzmann equation:

$$C_m = \frac{\alpha Q_{max} exp[\alpha(V_m - V_{pk})]}{\{1 + exp[\alpha(V_m - V_{pk})]\}^2} + C_{lin}$$

where a is the slope factor of the voltage-dependence of charge transfer, Q_{max} is the maximum charge transfer, V_m is the membrane potential, V_{pk} is the voltage at which the maximum charge movement is attained, and C_{lin} is the linear capacitance.

Hydrogen/Deuterium eXchange Mass Spectrometry (HDX-MS)

Hydrogen-Deuterium Exchange (HDX) combined with Liquid Chromatography-Mass Spectrometry (LC-MS) used purified dolphin Prestin samples. Table 1 provides biochemical and statistical details for HDX in this study per community recommendations [83]. HDX reactions, quench, injection, and LC-MS were all performed as previously described[24]. Briefly, HDX was initiated by diluting 2 µL of 20-25 µM prestin stock in an H_2O buffer into 28 µL of a matching deuterated buffer to reach 93% D-content. Labeling was conducted at room temperature at pD_{read} 7.1. For HDX on nanodisc-embedded prestin in the presence of αCD, the protein was pre-incubated with 10 mM αCD at room temperature for 15 min before dilution into a matching deuterated buffer containing 10 mM αCD to reach 73% D-content.

HDX was quenched at various times, ranging from 10 s to 27 h, by the addition of 30 µL of ice-chilled quench buffer containing 600 mM Glycine, 8 M urea, pH 2.5. For HDX on prestin in nanodisc, the quench buffer also included 3 µL of 0.8% GDN and 3 µL of 300 mg/ml aqueous suspension of ZrO2-coated silica (Sigma-Aldrich, reference no. 55261-U). Quenched reactions were immediately injected into the LC-MS system (Dionex UltiMate-3000 coupled with Thermo Q Exactive mass spectrometer). Protein digestion was performed online by a pepsin/FPXIII mixed protease column prepared in-house. Peptides were assigned by SearchGUI version 4.0.25, and HDX data was processed using HDExaminer 3.1 (Trajan) followed by manual curation.

Changes in free energy of unfolding (ΔΔG's) were calculated from the area between two deuterium uptake curves after correction for back-exchange[84]. Residue-level ΔΔG's were determined from a weighted average of peptide-level ΔΔG's, excluding the first two N-terminal residues due to rapid back-exchange. We note that, while most peptides exhibited near complete exchange within our labeling times, ΔΔG presented here is considered semi-quantitative, as precise quantification requires a broader and denser sampling of labeling times. Nonetheless, this approach effectively captures relative ΔΔG associated with changes in lipid environment or mutagenesis, and our major conclusions remain

independent of this fitting method. The deuteration differences shown in **Extended data Figure 5c,d** were adjusted for D-content but not for back-exchange.

Statistical analysis

Statistical significance (criteria, *$P < 0.05$; **$P<0.005$) between different electrophysiological conditions was determined using unpaired or paired Student's t-tests. R was used for all statistical analysis, and ggplot2[85] was used for plotting.

References.

1 Zheng, J. *et al.* Prestin is the motor protein of cochlear outer hair cells. *Nature* **405**, 149-155 (2000).

2 Liberman, M. C. *et al.* Prestin is required for electromotility of the outer hair cell and for the cochlear amplifier. *Nature* **419**, 300-304 (2002).

3 Dallos, P. *et al.* Prestin-based outer hair cell motility is necessary for mammalian cochlear amplification. *Neuron* **58**, 333-339 (2008).

4 Dong, X.-X. & Iwasa, K. Tension sensitivity of prestin: comparison with the membrane motor in outer hair cells. *Biophysical journal* **86**, 1201-1208 (2004).

5 Santos-Sacchi, J., Shen, W., Zheng, J. & Dallos, P. Effects of membrane potential and tension on prestin, the outer hair cell lateral membrane motor protein. *The Journal of physiology* **531**, 661-666 (2001).

6 Bavi, N., Cox, C. D., Nikolaev, Y. A. & Martinac, B. Molecular insights into the force-from-lipids gating of mechanosensitive channels. *Current Opinion in Physiology*, 100706 (2023).

7 Martinac, B. & Kung, C. The force-from-lipid principle and its origin, a 'what is true for E. coli is true for the elephant'refrain. *Journal of Neurogenetics* **36**, 44-54 (2022).

8 Dallos, P. & Fakler, B. Prestin, a new type of motor protein. *Nature Reviews Molecular Cell Biology* **3**, 104-111 (2002).

9 Ludwig, J. *et al.* Reciprocal electromechanical properties of rat prestin: the motor molecule from rat outer hair cells. *Proceedings of the National Academy of Sciences* **98**, 4178-4183 (2001).

10 Holley, M. & Ashmore, J. F. On the mechanism of a high-frequency force generator in outer hair cells isolated from the guinea pig cochlea. *Proceedings of the Royal society of London. Series B. Biological sciences* **232**, 413-429 (1988).

11 Brownell, W. E., Bader, C. R., Bertrand, D. & De Ribaupierre, Y. Evoked mechanical responses of isolated cochlear outer hair cells. *Science* **227**, 194-196 (1985).

12 Takahashi, S., Zhou, Y., Cheatham, M. A. & Homma, K. The pathogenic roles of the p. R130S prestin variant in DFNB61 hearing loss. *The Journal of physiology* **602**, 1199-1210 (2024).

13 Homma, K., Takahashi, S. & Cheatham, M. A. How much prestin motor activity is required for normal hearing? *Hearing research* **423**, 108376 (2022).

14 Dong, X.-x., Ospeck, M. & Iwasa, K. H. Piezoelectric reciprocal relationship of the membrane motor in the cochlear outer hair cell. *Biophysical journal* **82**, 1254-1259 (2002).

15 Fang, J., Izumi, C. & Iwasa, K. H. Sensitivity of prestin-based membrane motor to membrane thickness. *Biophysical journal* **98**, 2831-2838 (2010).

16 Kakehata, S. & Santos-Sacchi, J. Membrane tension directly shifts voltage dependence of outer hair cell motility and associated gating charge. *Biophysical journal* **68**, 2190-2197 (1995).

17 Izumi, C., Bird, J. E. & Iwasa, K. H. Membrane thickness sensitivity of prestin orthologs: the evolution of a piezoelectric protein. *Biophysical journal* **100**, 2614-2622 (2011).

18 Oliver, D. *et al.* Intracellular anions as the voltage sensor of prestin, the outer hair cell motor protein. *Science* **292**, 2340-2343 (2001).

19 Ashmore, J. Forward and reverse transduction in the mammalian cochlea. *Neuroscience Research Supplements* **12**, S39-S50 (1990).

20 Santos-Sacchi, J. Reversible inhibition of voltage-dependent outer hair cell motility and capacitance. *Journal of Neuroscience* **11**, 3096-3110 (1991).

21 Gorbunov, D. *et al.* Molecular architecture and the structural basis for anion interaction in prestin and SLC26 transporters. *Nature communications* **5**, 1-13 (2014).

22 Rybalchenko, V. & Santos-Sacchi, J. Anion control of voltage sensing by the motor protein prestin in outer hair cells. *Biophysical journal* **95**, 4439-4447 (2008).

23 Kakehata, S. & Santos-Sacchi, J. Effects of salicylate and lanthanides on outer hair cell motility and associated gating charge. *Journal of Neuroscience* **16**, 4881-4889 (1996).
24 Lin, X. *et al.* Folding of prestin's anion-binding site and the mechanism of outer hair cell electromotility. *eLife* **12**, RP89635 (2023).
25 Homma, K. & Dallos, P. Evidence that prestin has at least two voltage-dependent steps. *Journal of Biological Chemistry* **286**, 2297-2307 (2011).
26 Bavi, N. *et al.* The conformational cycle of prestin underlies outer-hair cell electromotility. *Nature* **600**, 553-558 (2021).
27 Futamata, H. *et al.* Cryo-EM structures of thermostabilized prestin provide mechanistic insights underlying outer hair cell electromotility. *Nature communications* **13**, 6208 (2022).
28 Ge, J. *et al.* Molecular mechanism of prestin electromotive signal amplification. *Cell* **184**, 4669-4679. e4613 (2021).
29 Butan, C. *et al.* Single particle cryo-EM structure of the outer hair cell motor protein prestin. *Nature communications* **13**, 290 (2022).
30 Cox, C. D., Bavi, N. & Martinac, B. Biophysical Principles of Ion-Channel-Mediated Mechanosensory Transduction. *Cell reports* **29**, 1-12, doi:10.1016/j.celrep.2019.08.075 (2019).
31 Li, Y., Liu, Z., Shi, P. & Zhang, J. The hearing gene Prestin unites echolocating bats and whales. *Current Biology* **20**, R55-R56 (2010).
32 Liu, Z., Qi, F.-Y., Xu, D.-M., Zhou, X. & Shi, P. Genomic and functional evidence reveals molecular insights into the origin of echolocation in whales. *Science advances* **4**, eaat8821 (2018).
33 Kuwabara, M. F. *et al.* Elevator-like movements of prestin mediate outer hair cell electromotility. *Nature communications* **14**, 7145 (2023).
34 Lenz, D. & Oliver, D. Progress in understanding the structural mechanism underlying prestin's electromotile activity. *Hearing Research* **423**, 108423 (2022).
35 Tippett, D. N., Breen, C., Butler, S. J., Sawicka, M. & Dutzler, R. Structural and functional properties of the transporter SLC26A6 reveal mechanism of coupled anion exchange. *eLife* **12**, RP87178 (2023).
36 Walter, J. D., Sawicka, M. & Dutzler, R. Cryo-EM structures and functional characterization of murine Slc26a9 reveal mechanism of uncoupled chloride transport. *eLife* **8**, e46986 (2019).
37 Chang, Y.-N. *et al.* Structural basis for functional interactions in dimers of SLC26 transporters. *Nature communications* **10**, 1-10 (2019).
38 Drew, D. & Boudker, O. Shared molecular mechanisms of membrane transporters. *Annual review of biochemistry* **85**, 543-572 (2016).
39 Garaeva, A. A. & Slotboom, D. J. Elevator-type mechanisms of membrane transport. *Biochemical Society transactions* **48**, 1227-1241 (2020).
40 Hu, W., Song, A. & Zheng, H. Substrate binding plasticity revealed by Cryo-EM structures of SLC26A2. *Nature Communications* **15**, 3616 (2024).
41 Chi, X. *et al.* Structural insights into the gating mechanism of human SLC26A9 mediated by its C-terminal sequence. *Cell discovery* **6**, 55 (2020).
42 Liu, Q. *et al.* Asymmetric pendrin homodimer reveals its molecular mechanism as anion exchanger. *Nature Communications* **14**, 3012 (2023).
43 Wang, L. *et al.* Mechanism of anion exchange and small-molecule inhibition of pendrin. *Nature Communications* **15**, 346 (2024).
44 Clark, M. D., Contreras, G. F., Bavi, N., Haller, P. R. & Perozo, E. An optimized protocol for on-column nanodisc formation. *Biophysical journal* **121**, 464a-465a (2022).
45 Sun, C., Zhu, H., Clark, S. & Gouaux, E. Cryo-EM structures reveal native GABAA receptor assemblies and pharmacology. *Nature* **622**, 195-201 (2023).
46 Raphael, R. M. Outer hair cell electromechanics as a problem in soft matter physics: Prestin, the membrane and the cytoskeleton. *Hearing Research* **423**, 108426 (2022).

47 Brownell, W. E., Spector, A. A., Raphael, R. M. & Popel, A. S. Micro- and nanomechanics of the cochlear outer hair cell. *Annu Rev Biomed Eng* **3**, 169-194, doi:10.1146/annurev.bioeng.3.1.169 (2001).

48 Organ, L. E. & Raphael, R. M. Application of fluorescence recovery after photobleaching to study prestin lateral mobility<? xpp qa?> in the human embryonic kidney cell. *Journal of biomedical optics* **12**, 021003-021003-021011 (2007).

49 Hopf, T. A. *et al.* The EVcouplings Python framework for coevolutionary sequence analysis. *Bioinformatics* **35**, 1582-1584 (2019).

50 Takahashi, S., Zhou, Y., Kojima, T., Cheatham, M. A. & Homma, K. Prestin's fast motor kinetics is essential for mammalian cochlear amplification. *Proceedings of the National Academy of Sciences* **120**, e2217891120 (2023).

51 Bai, J.-P. *et al.* Chloride binding to prestin does not influence very high-frequency complex nonlinear capacitance (cNLC) in the mouse outer hair cell. *bioRxiv*, 2024.2001. 2029.577264 (2024).

52 Bai, J.-P. *et al.* Chloride binding does not influence prestin motor speed at very high frequencies in the mouse outer hair cell. *Structure* (2025).

53 Geertsma, E. R. & Oliver, D. SLC26 anion transporters. *Anion Channels and Transporters*, 319-360 (2023).

54 Beurg, M., Tan, X. & Fettiplace, R. A prestin motor in chicken auditory hair cells: active force generation in a nonmammalian species. *Neuron* **79**, 69-81 (2013).

55 He, D. Z. *et al.* Chick hair cells do not exhibit voltage-dependent somatic motility. *The Journal of physiology* **546**, 511-520 (2003).

56 Fettiplace, R. & Beurg, M. The Mechanisms of Frequency Tuning in Gecko Auditory Hair Cells. *Hearing Research*, 109186 (2025).

57 Schaechinger, T. J. & Oliver, D. Nonmammalian orthologs of prestin (SLC26A5) are electrogenic divalent/chloride anion exchangers. *Proceedings of the National Academy of Sciences* **104**, 7693-7698 (2007).

58 Tan, X. *et al.* From zebrafish to mammal: functional evolution of prestin, the motor protein of cochlear outer hair cells. *Journal of neurophysiology* **105**, 36-44 (2011).

59 Tang, J., Pecka, J. L., Fritzsch, B., Beisel, K. W. & He, D. Z. Lizard and frog prestin: evolutionary insight into functional changes. *PloS one* **8**, e54388 (2013).

60 Vavakou, A., Cooper, N. P. & van der Heijden, M. The frequency limit of outer hair cell motility measured in vivo. *eLife* **8**, e47667 (2019).

61 Altoè, A. & Shera, C. A. The long outer-hair-cell RC time constant: A feature, not a bug, of the Mammalian Cochlea. *Journal of the Association for Research in Otolaryngology* **24**, 129-145 (2023).

62 van der Heijden, M. & Vavakou, A. Rectifying and sluggish: outer hair cells as regulators rather than amplifiers. *Hearing Research* **423**, 108367 (2022).

63 Santos-Sacchi, J., Bai, J.-P. & Navaratnam, D. Megahertz sampling of prestin (SLC26a5) voltage-sensor charge movements in outer hair cell membranes reveals ultrasonic activity that may support electromotility and cochlear amplification. *Journal of Neuroscience* **43**, 2460-2468 (2023).

64 Dewey, J. B., Altoè, A., Shera, C. A., Applegate, B. E. & Oghalai, J. S. Cochlear outer hair cell electromotility enhances organ of Corti motion on a cycle-by-cycle basis at high frequencies in vivo. *Proceedings of the National Academy of Sciences* **118**, e2025206118 (2021).

65 He, D. Z., Jia, S. & Dallos, P. Prestin and the dynamic stiffness of cochlear outer hair cells. *Journal of Neuroscience* **23**, 9089-9096 (2003).

66 Rabbitt, R. D. Analysis of outer hair cell electromechanics reveals power delivery at the upper-frequency limits of hearing. *Journal of The Royal Society Interface* **19**, 20220139 (2022).

67 Kirchhofer, A. *et al.* Modulation of protein properties in living cells using nanobodies. *Nature structural & molecular biology* **17**, 133-138 (2010).
68 Cordingley, M. G., Register, R. B., Callahan, P., Garsky, V. M. & Colonno, R. Cleavage of small peptides in vitro by human rhinovirus 14 3C protease expressed in Escherichia coli. *Journal of virology* **63**, 5037-5045 (1989).
69 Alvarez, F. J. D., Orelle, C. & Davidson, A. L. Functional reconstitution of an ABC transporter in nanodiscs for use in electron paramagnetic resonance spectroscopy. *Journal of the American Chemical Society* **132**, 9513-9515 (2010).
70 Kimanius, D., Dong, L., Sharov, G., Nakane, T. & Scheres, S. H. New tools for automated cryo-EM single-particle analysis in RELION-4.0. *Biochemical Journal* **478**, 4169-4185 (2021).
71 Scheres, S. H. RELION: implementation of a Bayesian approach to cryo-EM structure determination. *Journal of structural biology* **180**, 519-530 (2012).
72 Punjani, A., Rubinstein, J. L., Fleet, D. J. & Brubaker, M. A. cryoSPARC: algorithms for rapid unsupervised cryo-EM structure determination. *Nature methods* **14**, 290-296 (2017).
73 Punjani, A., Zhang, H. & Fleet, D. J. Non-uniform refinement: adaptive regularization improves single-particle cryo-EM reconstruction. *Nature methods* **17**, 1214-1221 (2020).
74 Mirdita, M. *et al.* ColabFold: making protein folding accessible to all. *Nature methods* **19**, 679-682 (2022).
75 Afonine, P. V. *et al.* Real-space refinement in PHENIX for cryo-EM and crystallography. *Biological Crystallography* **74**, 531-544 (2018).
76 Emsley, P., Lohkamp, B., Scott, W. G. & Cowtan, K. Features and development of Coot. *Biological crystallography* **66**, 486-501 (2010).
77 Croll, T. I. ISOLDE: a physically realistic environment for model building into low-resolution electron-density maps. *Biological Crystallography* **74**, 519-530 (2018).
78 Jo, S., Vargyas, M., Vasko-Szedlar, J., Roux, B. & Im, W. PBEQ-Solver for online visualization of electrostatic potential of biomolecules. *Nucleic acids research* **36**, W270-W275 (2008).
79 Jo, S., Kim, T., Iyer, V. G. & Im, W. CHARMM-GUI: a web-based graphical user interface for CHARMM. *Journal of computational chemistry* **29**, 1859-1865 (2008).
80 Meng, E. C. *et al.* UCSF ChimeraX: Tools for structure building and analysis. *Protein Science* **32**, e4792 (2023).
81 Lindau, M. & Neher, E. Patch-clamp techniques for time-resolved capacitance measurements in single cells. *Pflügers Archiv* **411**, 137-146 (1988).
82 Homma, K., Duan, C., Zheng, J., Cheatham, M. A. & Dallos, P. The V499G/Y501H mutation impairs fast motor kinetics of prestin and has significance for defining functional independence of individual prestin subunits. *Journal of Biological Chemistry* **288**, 2452-2463 (2013).
83 Masson, G. R. *et al.* Recommendations for performing, interpreting and reporting hydrogen deuterium exchange mass spectrometry (HDX-MS) experiments. *Nature methods* **16**, 595-602 (2019).
84 Hamuro, Y. Quantitative hydrogen/deuterium exchange mass spectrometry. *Journal of the American Society for Mass Spectrometry* **32**, 2711-2727 (2021).
85 Villanueva, R. A. M. & Chen, Z. J. (Taylor & Francis, 2019).

Extended data figures

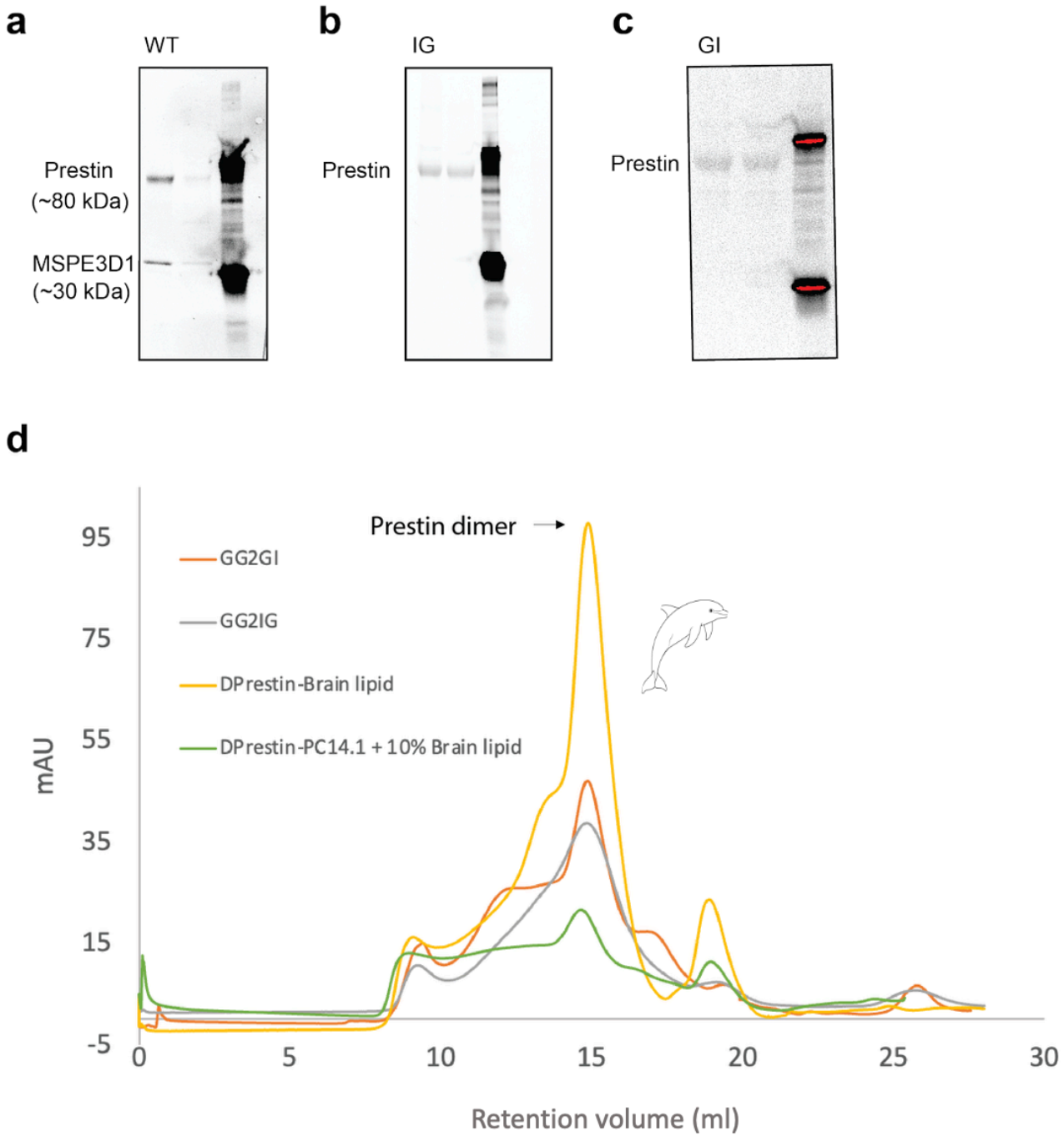

Extended Data Fig. 1: SDS-PAGE and size-exclusion chromatography (SEC) HPLC of purified dolphin prestin mutant in detergent and nanodiscs. a-c) SDS-PAGE gel of purified prestin samples. Only representative purification samples are shown for clarity. Prestin monomer elutes at ~80 kDa (~160 kDa as a dimer). **d**) Purification in detergent and nanodiscs results in a monodisperse peak using a Superose 6 column, which was subsequently collected and concentrated for sample freezing.

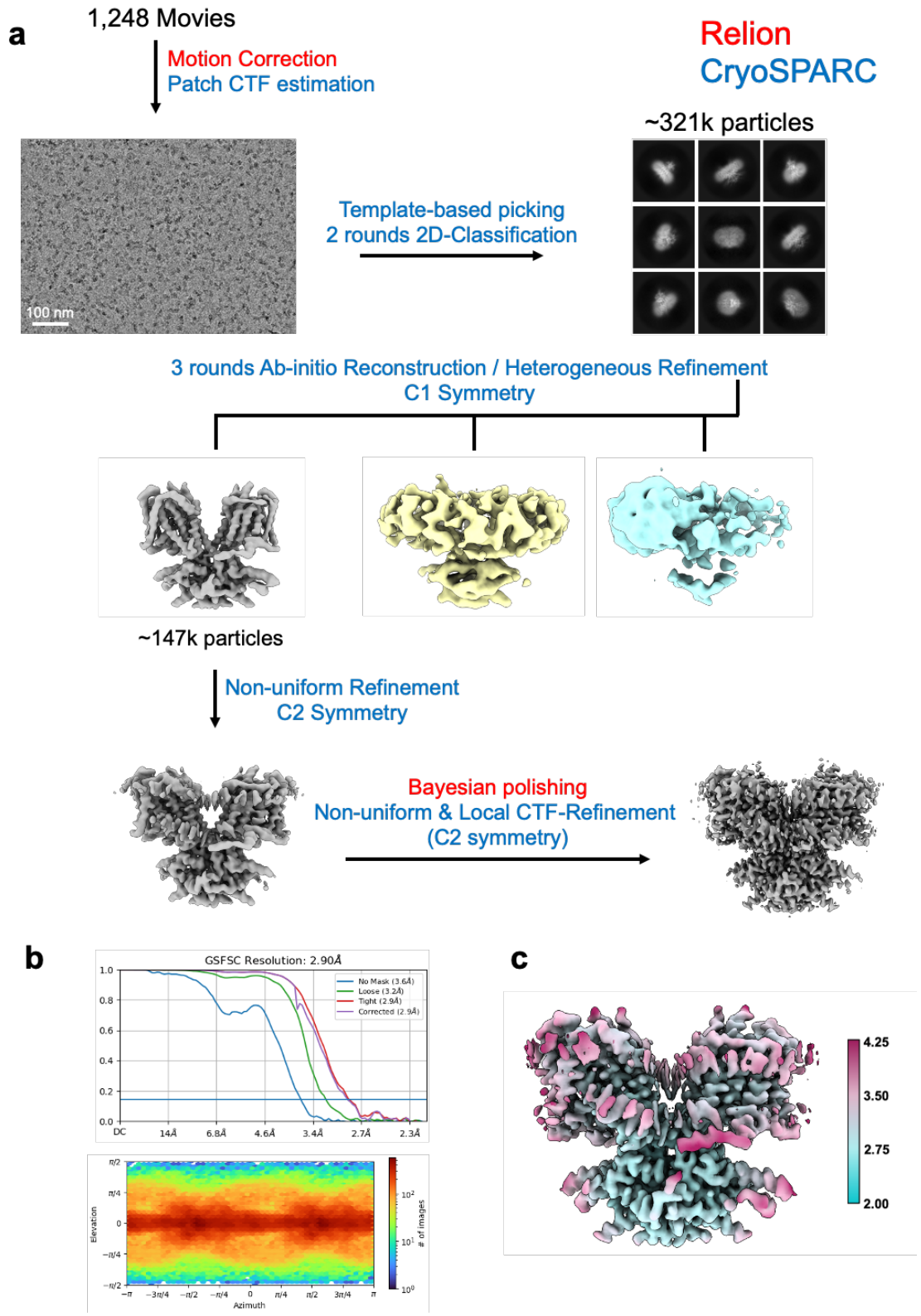

Extended Data Fig. 2: Cryo-EM workflow for dolphin prestin in brain-lipid extract and MSPE3D1 nanodiscs (See Methods). a) Data processing was performed using Relion and CryoSPARC. Motion correction and Patch CTF estimation were followed by template-based particle picking and two rounds of 2D classification. Three rounds of ab-initio reconstruction and heterogeneous refinement were performed with C1 symmetry, followed by non-uniform refinement with C2 symmetry. Bayesian

polishing and local CTF refinement further improved map quality, (**b**) yielding a final 2.90 Å nominal resolution reconstruction, as shown in the FSC and angular distribution plots. **c)** Local resolution estimation for the final reconstruction.

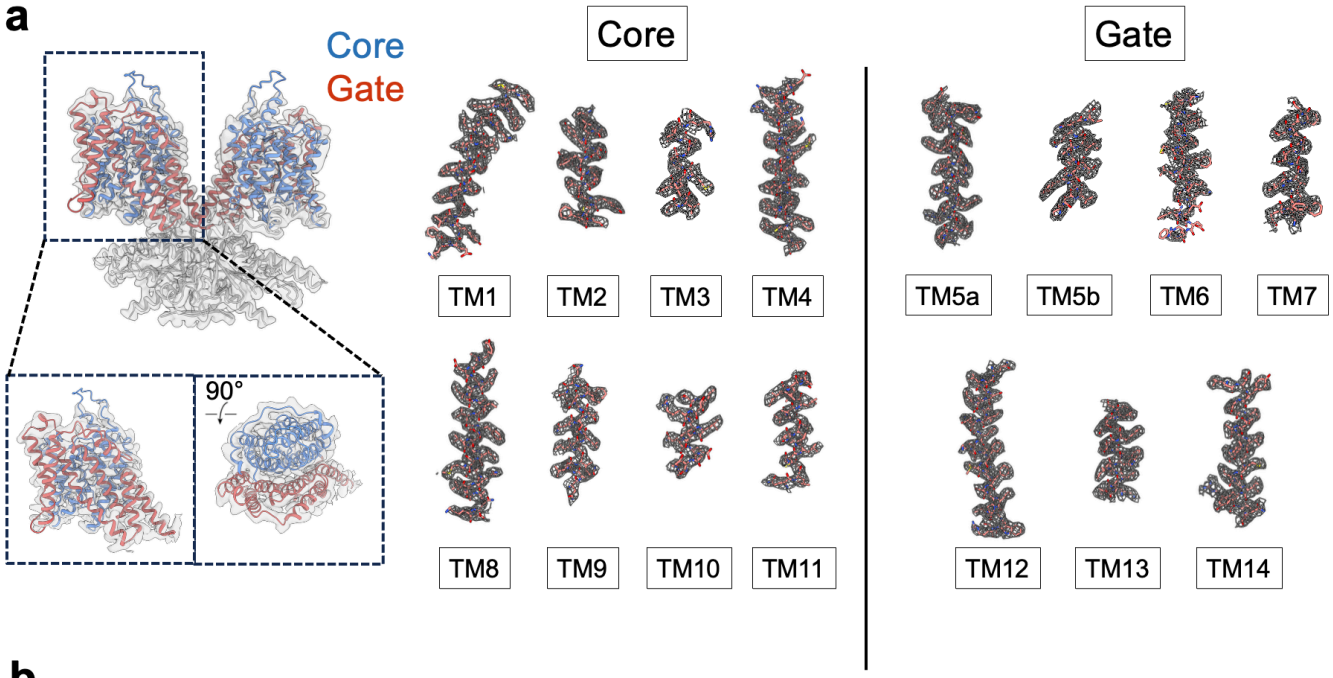

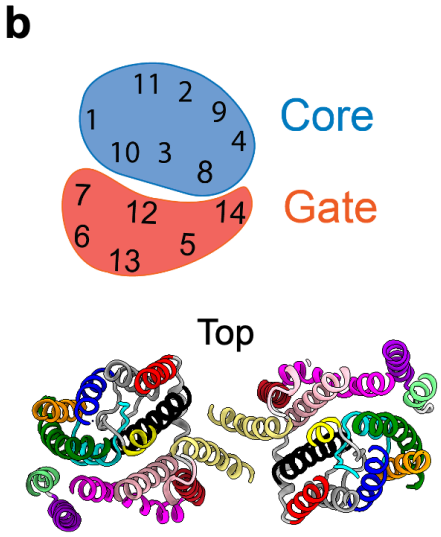

Domain	Helix	Residue Range	Color	Description
Core	1	76-104	Green	TM helix 1
	2	110-126	Blue	TM helix 2
	3	138-150	Yellow	TM helix 3
	4	169-195	Red	TM helix 4
	8	340-365	Black	TM helix 8
	9	372-391	Dark Grey	TM helix 9
	10	390-410	Cyan	TM helix 10
	11	411-428	Orange	TM helix 11
Gate	5	207-230, 241-254	Pink	TM helix 5 (a,b)
	6	259-283	Dark Violet	TM helix 6
	7	290-307	Light Green	TM helix 7
	12	437-464	Magenta	TM helix 12
	13	466-481	Brown	TM helix 13
	14	484-504	Khaki	TM helix 14

Extended Data Fig. 3: Model-to-density fit and architecture of dolphin prestin as a homodimer. Dolphin prestin in brain lipid extract nanodiscs is shown as an example. **a**) Density fit for the transmembrane region of dolphin prestin in brain lipid nanodiscs. **b**) Residue mapping for TM helices (TM1-TM14) in the core and gate domains of prestin.

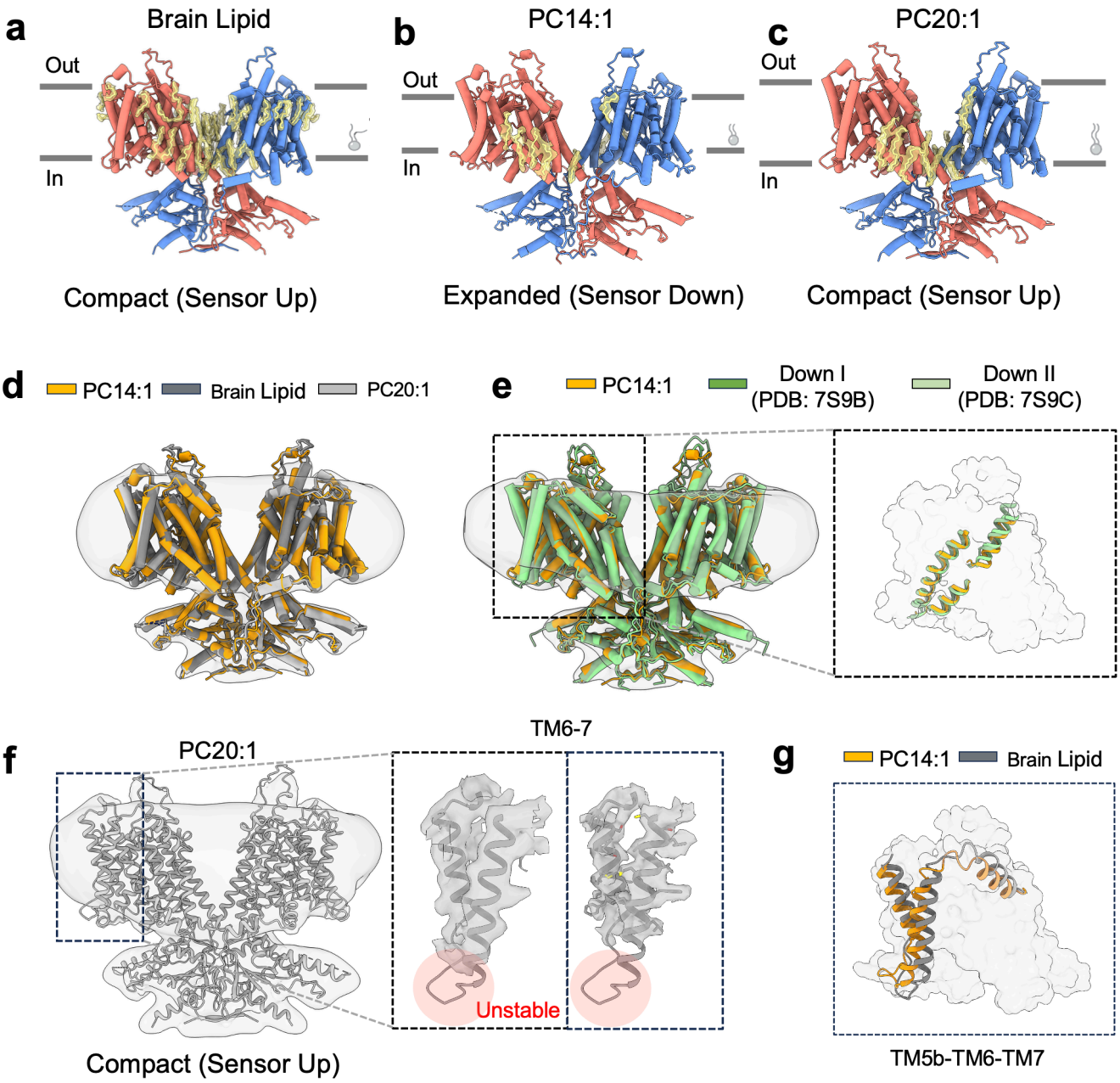

Extended Data Fig. 4. Models of structural lipids based on density maps for dolphin prestin in nanodiscs with various compositions, including (**a**) brain lipid extract, (**b**) PC14:1, and (**c**) PC20:1 (see Methods for detailed composition). Several lipid-like densities were observed at the periphery of prestin's TMD in the brain lipid nanodisc, indicating its intimate interactions with the surrounding bilayer. The putative lipids were modeled as hydrocarbon chains of varying lengths. For instance, in PC14:1 nanodiscs, putative lipids were modeled as C14 hydrocarbon chains, only into densities of approximately the proper length, whereas in PC20:1 nanodiscs, they were modeled accordingly. **d**) The overlay of the three dolphin structures (**a-c**) in cartoon representation. **e**) Structural overlay of the structure in PC14:1 nanodiscs with previously published structures in the "Down" conformation. **f**) Depiction of the cryo-EM density for TM6-7 in PC20:1 nanodiscs. The lack of density highlights the

structural flexibility in those helices. **g**) Transmembrane helices TM6-TM7 undergo significant conformational changes in different nanodisc conditions, bending at the gating region to accommodate varying bilayer thickness. This is accompanied by the adaptation of TM5b (depicted in light orange and light grey)

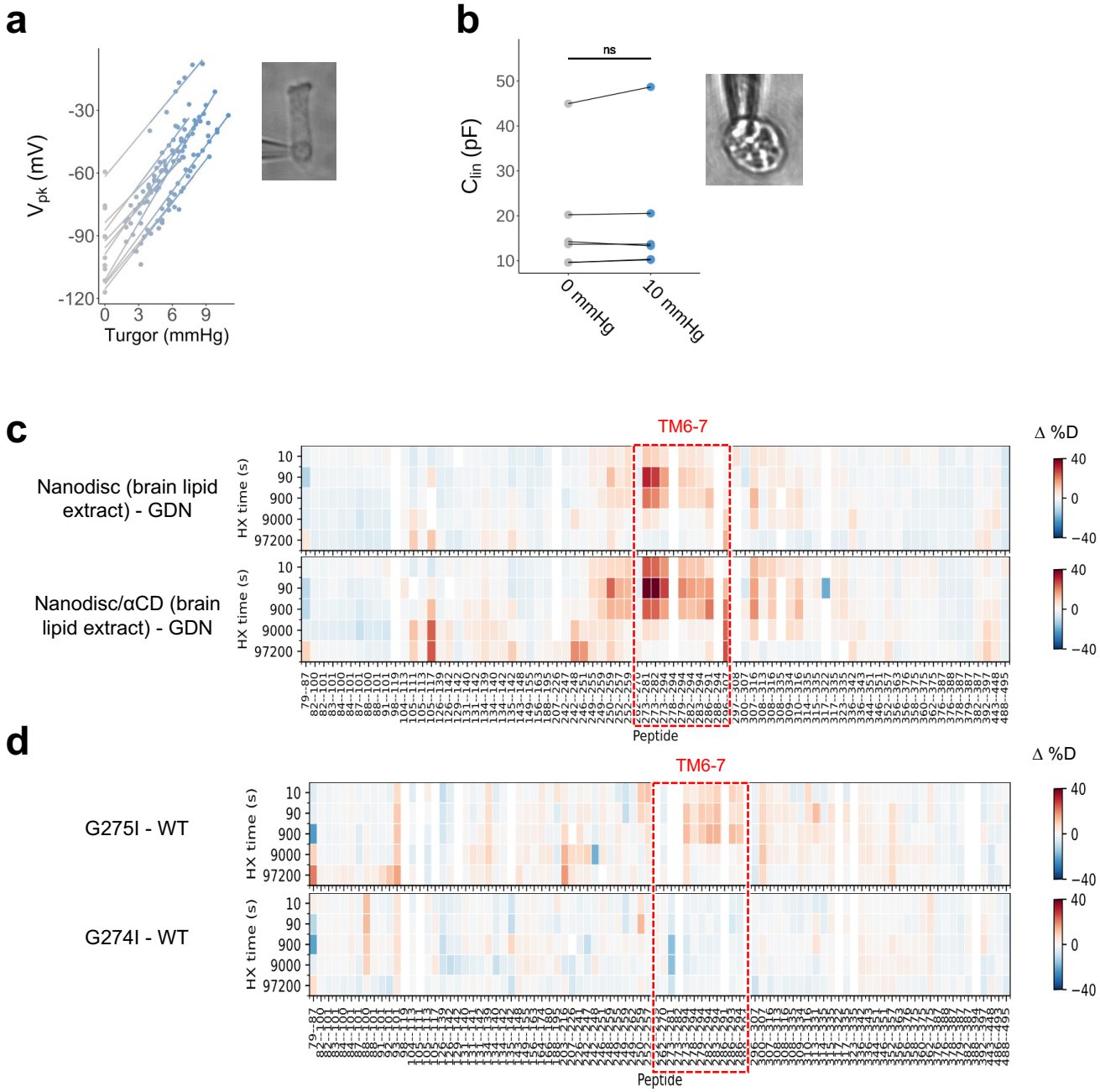

Extended Data Fig. 5: Whole-cell patch-clamp electrophysiology of prestin.a) Change in Vpk of adult mouse hair cells in response to turgor pressure (membrane tension; n=10). **b**) Change in linear capacitance upon increasing turgor pressure in HEK-293 cells overexpressing dolphin prestin in whole-cell mode. In each case, linear capacitance increases with increasing turgor pressure inside the cell by applying positive pressure (10 mmHg) through the pipette (n=6). **c,d**) HDX-MS data shows that TM6-7 region dynamics in response to changes in the lipid environment. Heatmaps show differences in deuteration levels at each labeling time for all TMD peptides measured in one of the following conditions

compared to wild-type GDN-solubilized prestin: (c) WT prestin in porcine brain total lipid nanodisc with (top) and without (bottom) 10 mM αCD, (d) GDN-solubilized G275I (top) and G274I (bottom) mutant.

5

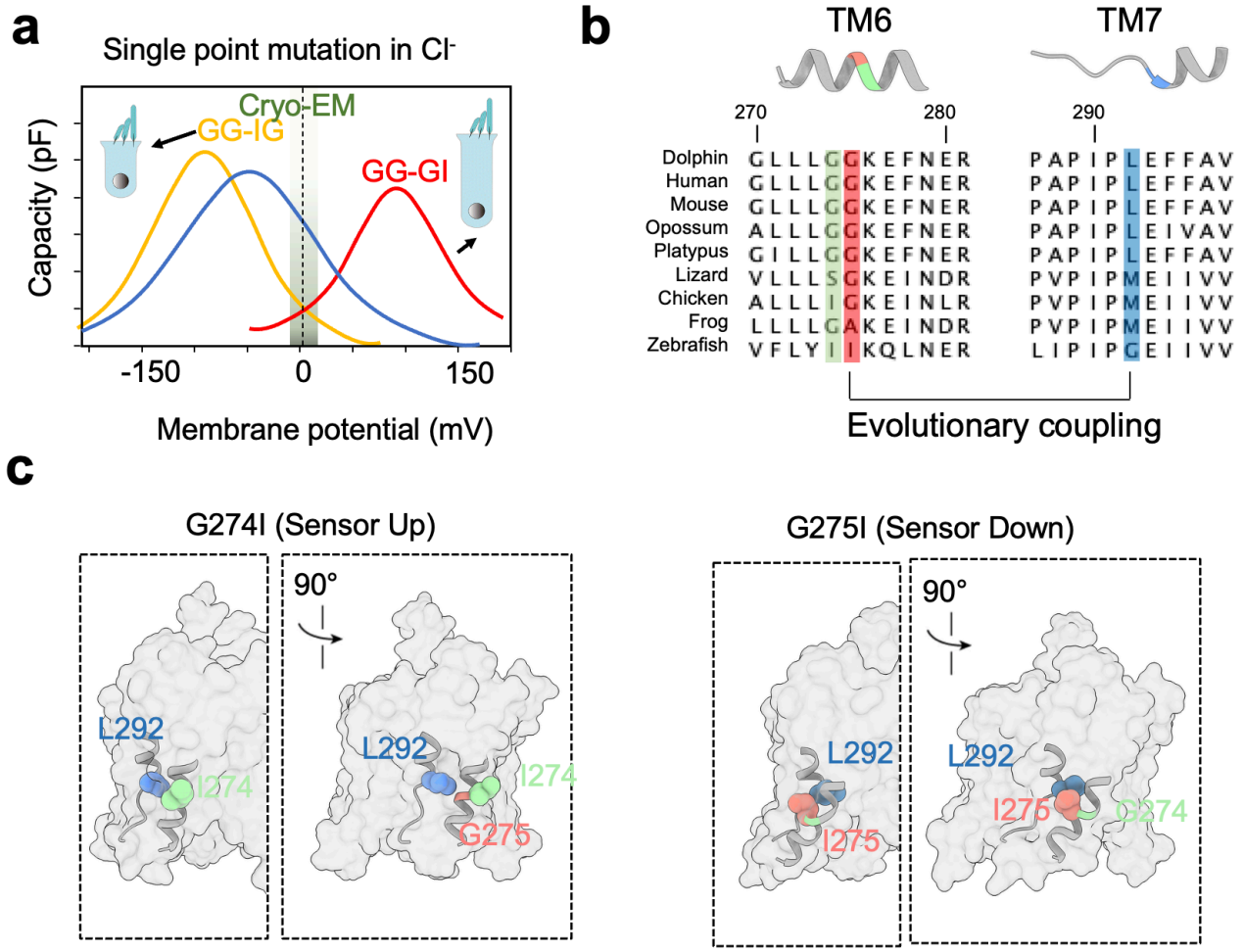

Extended Data Fig. 6: TM6-7 helices function as electromotility "elbows," responding to membrane forces. These helices contain a series of glycine residues critical for prestin's motor function and mechanosensitivity. Mutations in these residues impact both mechanosensitivity and voltage sensitivity of the protein[27]. **a)** Substitution of G274 to isoleucine results in a leftward shift of the nonlinear capacitance (NLC), whereas G275I causes a rightward shift[27]. **b,c)** Evolutionary coupling of TM6 and TM7 helices. Structural analysis of these mutants in chloride-bound and detergent-solubilized conditions reveals that the bulkiness and entropic hindrance of L292 interactions (located on TM7) with these glycine residues (on TM6) may regulate the bending dynamics of TM6-TM7, influencing prestin's conformational dynamics in response to both voltage and mechanical force.

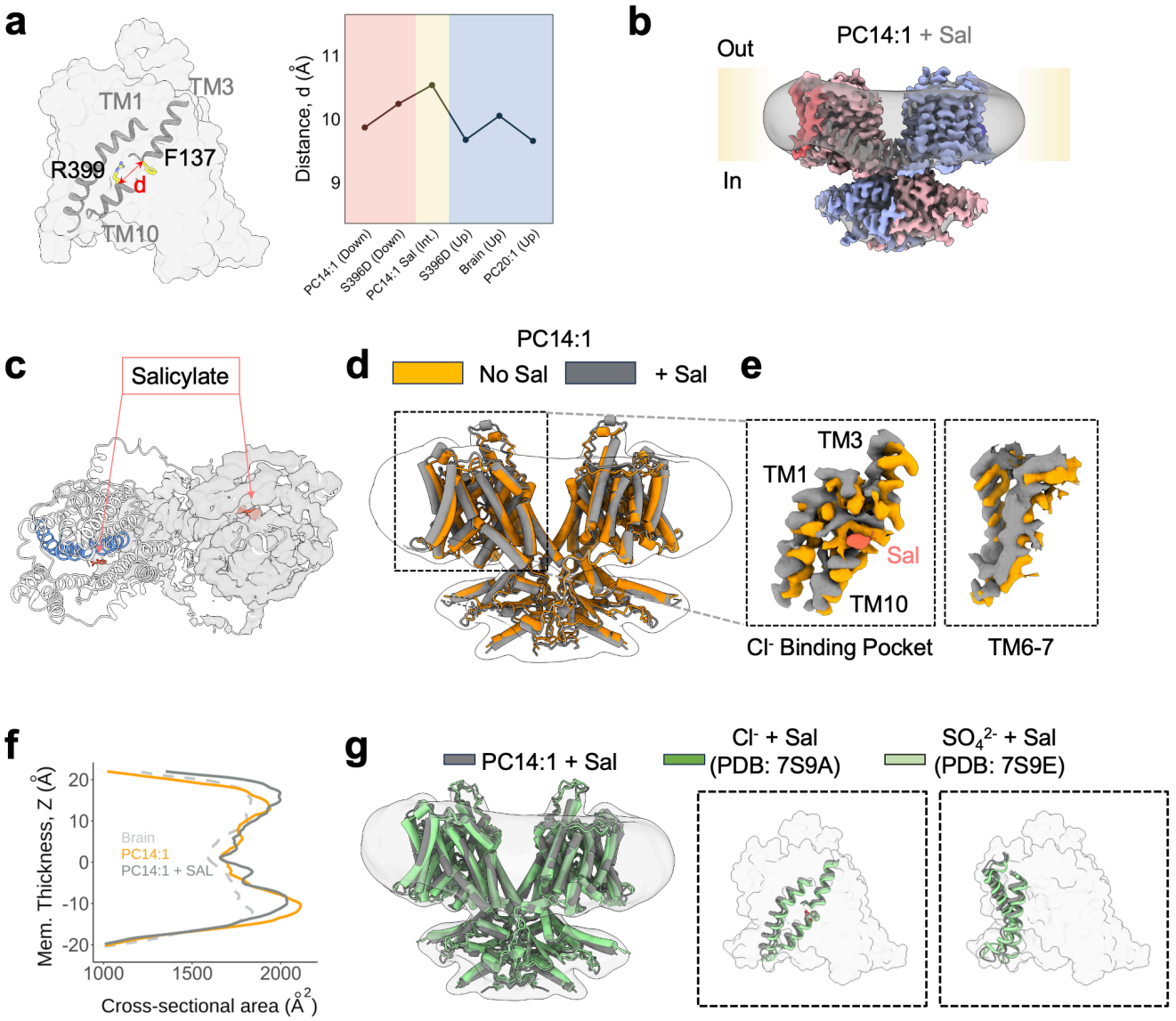

Extended Data Fig. 7: Dynamics of anion binding site size in different states and when occluded with Cl^- versus salicylate. a) *d* represents the distance between the alpha carbon of R399 and F137, which approximately corresponds to the diameter of the anion binding site. The changes in *d* are <1 Å, but the distance is largest when the anion binding site is occluded with salicylate. **b**) Structure of dolphin prestin in a PC14:1 nanodisc in the presence of 10 mM salicylate (MSPE3D1). **c**) Structural comparison of dolphin prestin in PC14:1 nanodiscs with and without salicylate. **d**) While the sensor domain remains similar in both structures, the largest area change in the PC14:1-salicylate structure is primarily due to the outward kinking of TM6-TM7 at the protein-lipid interface. (**e**) Structural comparison of the anion binding site of dolphin prestin in PC14:1 nanodiscs with and without salicylate. (**f**) While the sensor domain remains similar in both structures, the largest area change in the PC14:1 structure is primarily

due to the outward kinking of TM6-TM7 at the protein-lipid interface. **g**) Structural comparison of PC14:1 with Salicylate with previously published structures in detergent (PDB IDs: 7S9A and 7S9E).

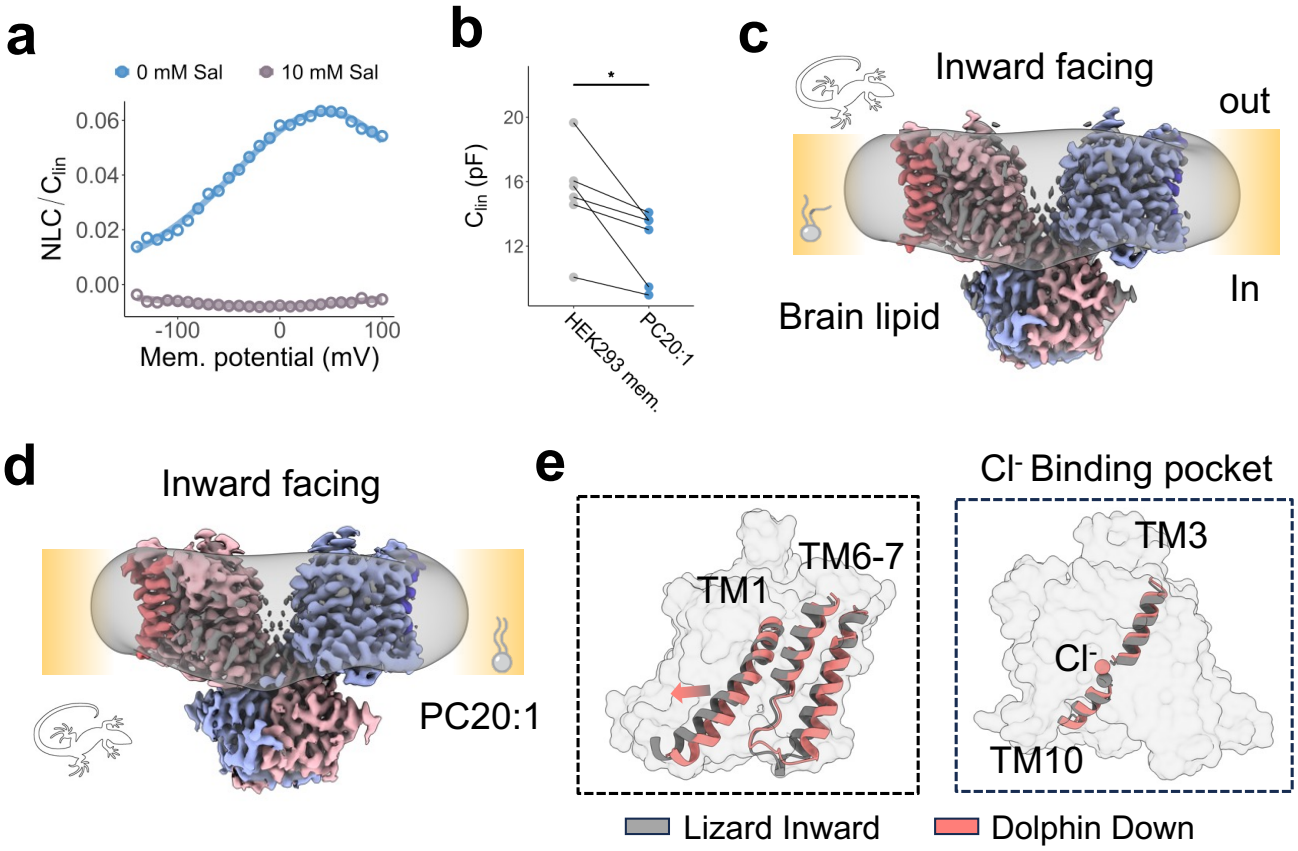

Extended Data Fig. 8: Functional and structural properties of Lizard SLC26A5. a) Whole-cell patch-clamp electrophysiology of Lizard SLC26A5 overexpressed in HEK293 cells. 10 mM salicylate flattens the NLC of Lizard SLC26A5, similar to dolphin prestin. (n = 7) **b**) Changes in linear capacitance after injection of PC20:1, supporting the idea that lizard SLC26A5 is unresponsive to changes in lipid thickness after equilibration (> 5 minutes). **c**) Density for inward-facing Lizard SLC26A5 in brain lipid extract and (**d**) PC20:1. No significant difference is observed between the two structures in these conditions. **e**) Downward-facing structure of Lizard SLC26A5 compared to dolphin prestin in the expanded (Sensor Down state), obtained under PC14:1 lipid nanodiscs. The anion binding site (the voltage sensor) is in the same state. The main differences are in in the TM1 (core domain) and TM6-7 (gate) regions.

Supplementary figures

a

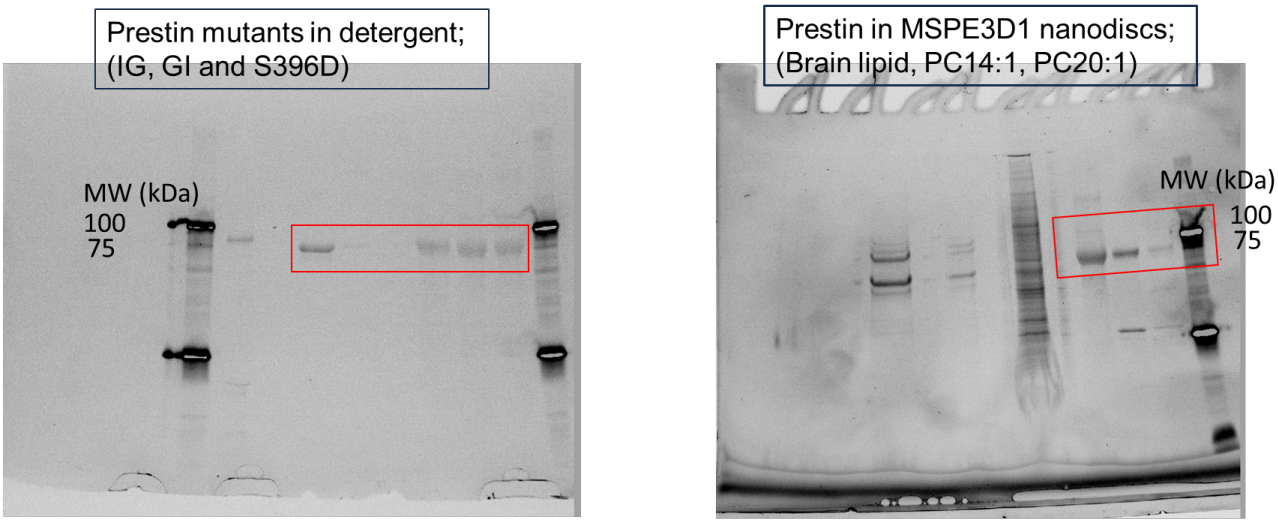

b

Dataset	WT, GDN	WT, nanodisc (porcine brain total lipid extract)	WT, nanodisc (porcine brain total lipid extract) + αCD	WT, nanodisc (PC20/porcine brain total lipid extract)	WT, nanodisc (PC20/porcine brain total lipid extract) + αCD	G274I, GDN	G275I, GDN
HDX reaction details	20 mM Tris, 360 mM NaCl, 3 mM DTT, 1 mM EDTA, 0.02% GDN. pD_{read} 7.1, 25 °C	20 mM Tris, 150 mM NaCl. pD_{read} 7.1, 25 °C	20 mM Tris, 150 mM NaCl, 10 mM αCD. pD_{read} 7.1, 25 °C	20 mM Tris, 150 mM NaCl. pD_{read} 7.1, 25 °C	20 mM Tris, 150 mM NaCl, 10 mM αCD. pD_{read} 7.1, 25 °C	20 mM Tris, 360 mM NaCl, 3 mM DTT, 1 mM EDTA, 0.02% GDN. pD_{read} 7.1, 25 °C	20 mM Tris, 360 mM NaCl, 3 mM DTT, 1 mM EDTA, 0.02% GDN. pD_{read} 7.1, 25 °C
HDX time course (*: replicated)	10s*, 30s, 90s*, 5min, 15min*, 45min, 150min*, 27h*	10s, 90s, 15min, 150min, 27h	10s, 90s, 15min, 150min, 27h	10s, 90s, 15min, 150min, 27h	10s, 90s, 15min, 150min, 27h	10s*, 90s*, 5min, 15min*, 150min*, 27h*	10s*, 90s*, 15min*, 150min*, 27h*
HDX control samples	Non-deuterated control; in-exchange control; maximally labeled control						
In- and back-exchange, mean/IQR (TMD peptides only)	In-exchange: 2.5% / 2.2%; back-exchange: 25% / 13%						
No. of peptides (TMD only)	92	74	74	72	71	84	79
Sequence coverage (TMD only)	75%	59%	59%	63%	63%	73%	73%
Average peptide length/redundancy (TMD peptides only)	11.7/2.6	11.5/2.1	11.5/2.1	11.7/2.0	11.7/2.0	11.9/2.4	12.1/2.3
Replicates	2 (Biological)	1	1	1	1	2 (Technical)	2 (Technical)
Repeatability (SD of the Δ%D/Δ#D between duplicates) (TMD peptides only)	0.69%/ 0.06 Da	N/A	N/A	N/A	N/A	1.77%/0.16 Da	1.99%/0.17 Da

Supplementary Figure 1: The uncropped SDS-page of dolphin Prestin purification used in Extended data fig. 1. The bands in the red rectangle are Dolphin prestin. **b**) Biochemical and statistical details for HDX-MS.

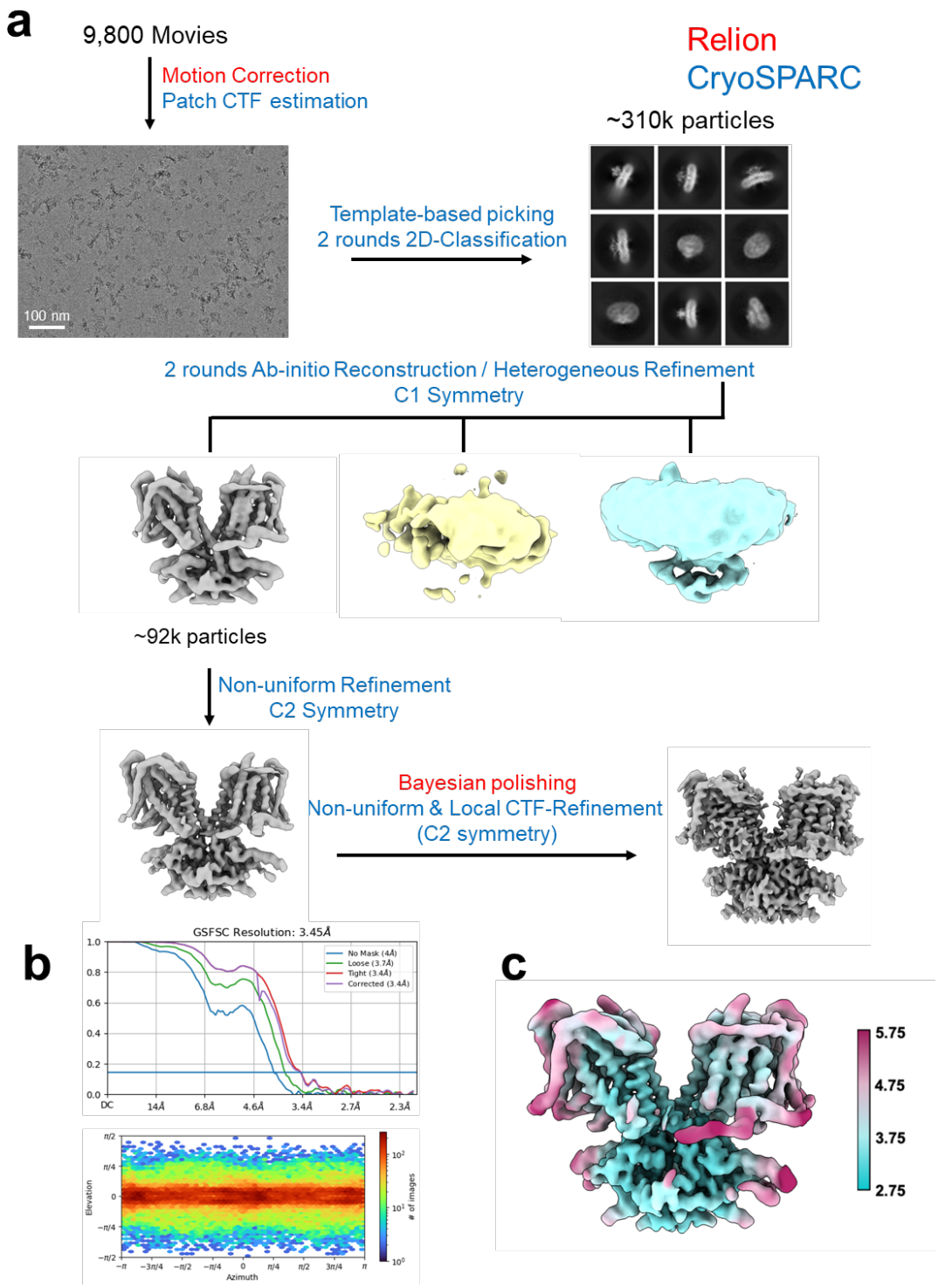

Supplementary Figure 2: Cryo-EM workflow for dolphin prestin in PC14:1 lipids and MSPE3D1 nanodiscs. a) Data processing was conducted using Relion and CryoSPARC. The workflow included motion correction and Patch CTF estimation, followed by template-based particle picking and two rounds of 2D classification. Two rounds of ab-initio reconstruction and heterogeneous refinement were performed under C1 symmetry, succeeded by non-uniform refinement with C2 symmetry. Bayesian polishing and local CTF refinement were applied to enhance map quality, (b) resulting in a final

reconstruction at 3.45 Å resolution. The FSC and angular distribution plots illustrate the achieved nominal resolution and particle orientation. **c)** Local resolution estimation for the final reconstruction.

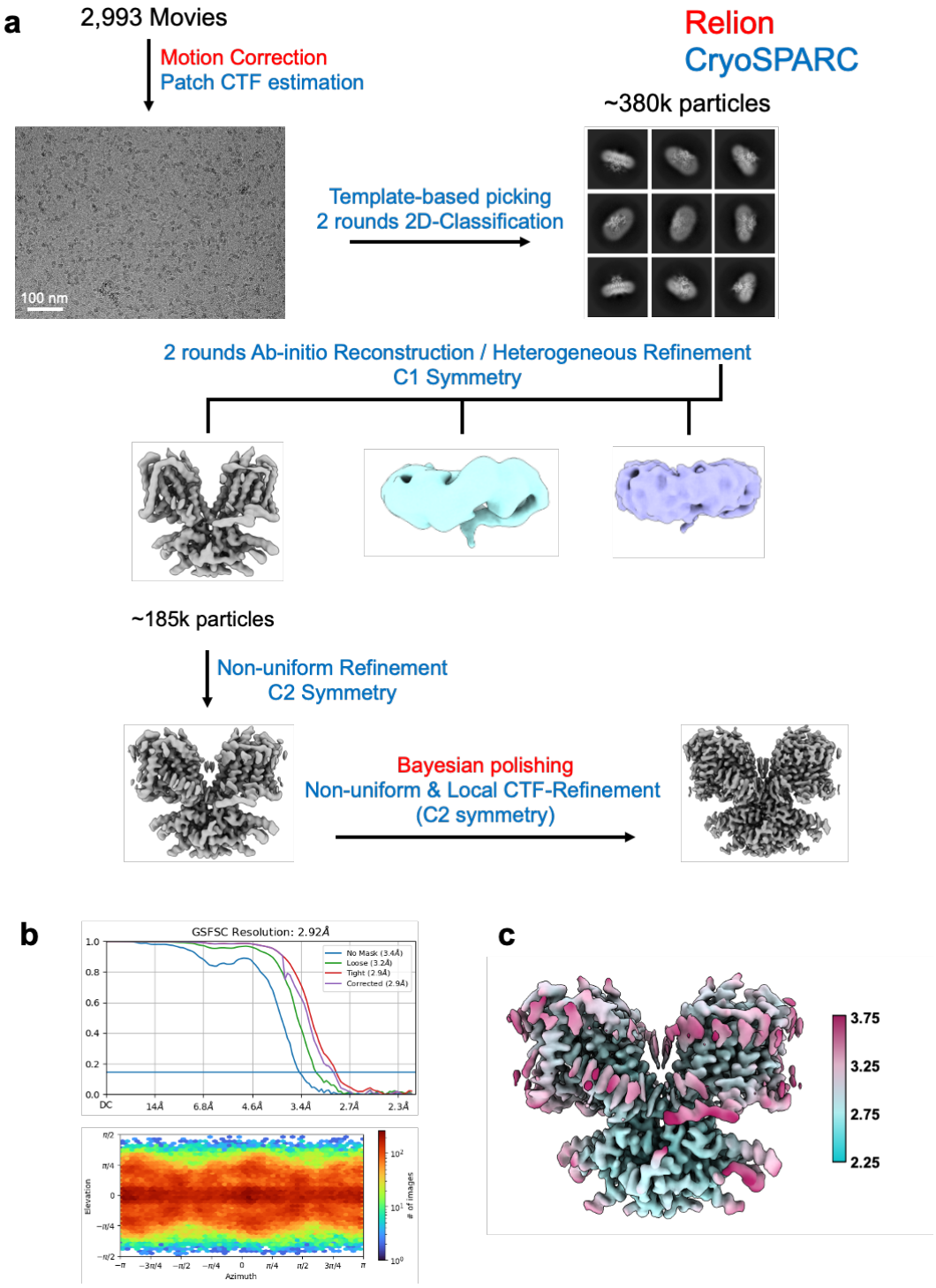

Supplementary Figure 3: Cryo-EM workflow for dolphin prestin G274I in detergent (GDN). a) Data processing was conducted using Relion and CryoSPARC. The workflow included motion correction and Patch CTF estimation, followed by template-based particle picking and two rounds of 2D classification. Two rounds of ab-initio reconstruction and heterogeneous refinement were performed under C1 symmetry, succeeded by non-uniform refinement with C2 symmetry. Bayesian polishing and local CTF refinement were applied to enhance map quality, (**b**) resulting in a final reconstruction at 2.92 Å resolution. The FSC and angular distribution plots illustrate the achieved nominal resolution and particle orientation. **c)** Local resolution estimation for the final reconstruction.

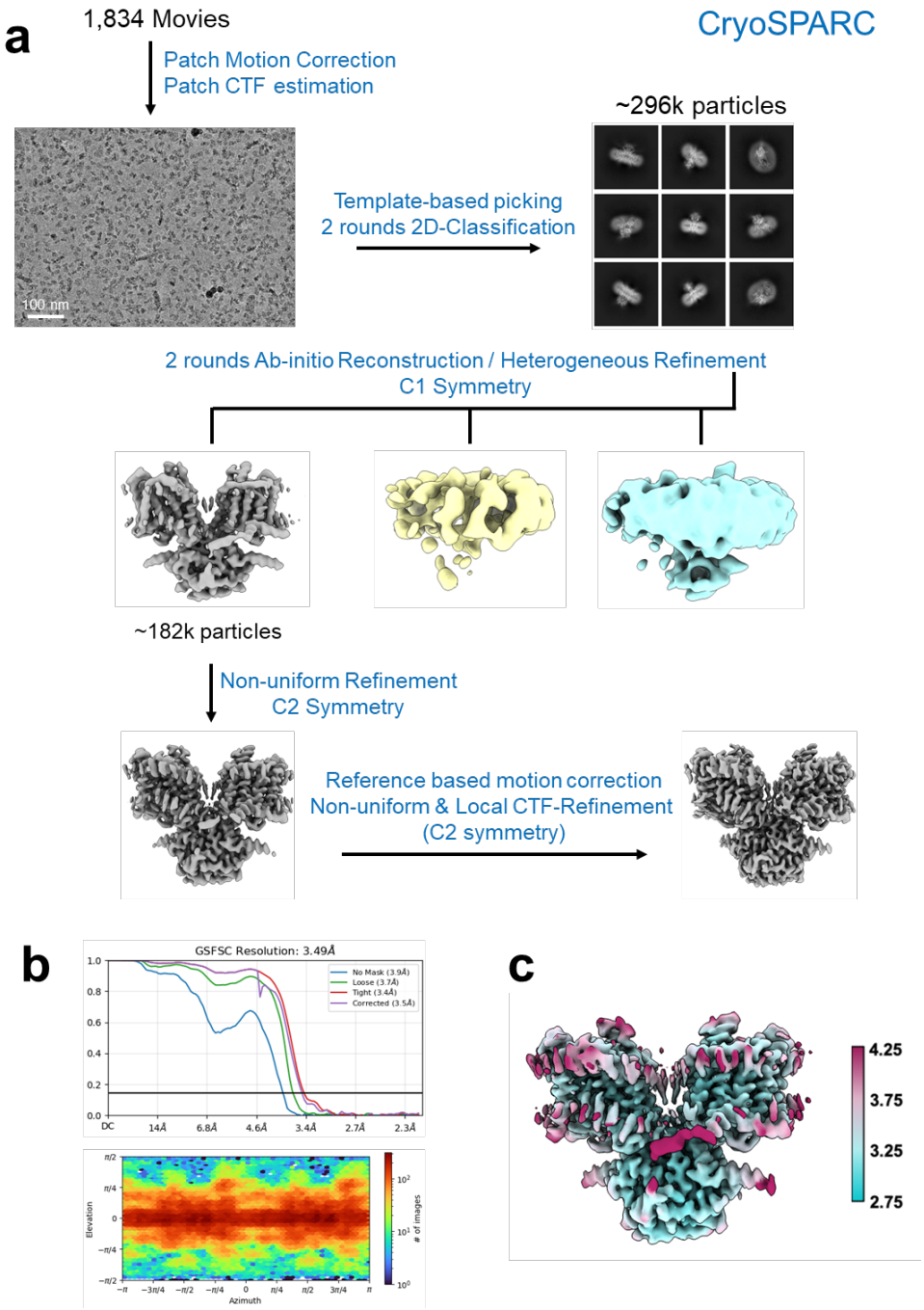

Supplementary Figure 4: Cryo-EM workflow for lizard SLC26A5 in brain lipid nanodiscs. a) Data processing was conducted using Relion and CryoSPARC. The workflow included motion correction and Patch CTF estimation, followed by template-based particle picking and two rounds of 2D classification. Two rounds of ab-initio reconstruction and heterogeneous refinement were performed under C1 symmetry, succeeded by non-uniform refinement with C2 symmetry. Bayesian polishing and local CTF refinement were applied to enhance map quality, (**b**) resulting in a final reconstruction at 3.49 Å nominal resolution. The FSC and angular distribution plots illustrate the achieved nominal resolution and particle orientation. **c)** Local resolution estimation for the final reconstruction.

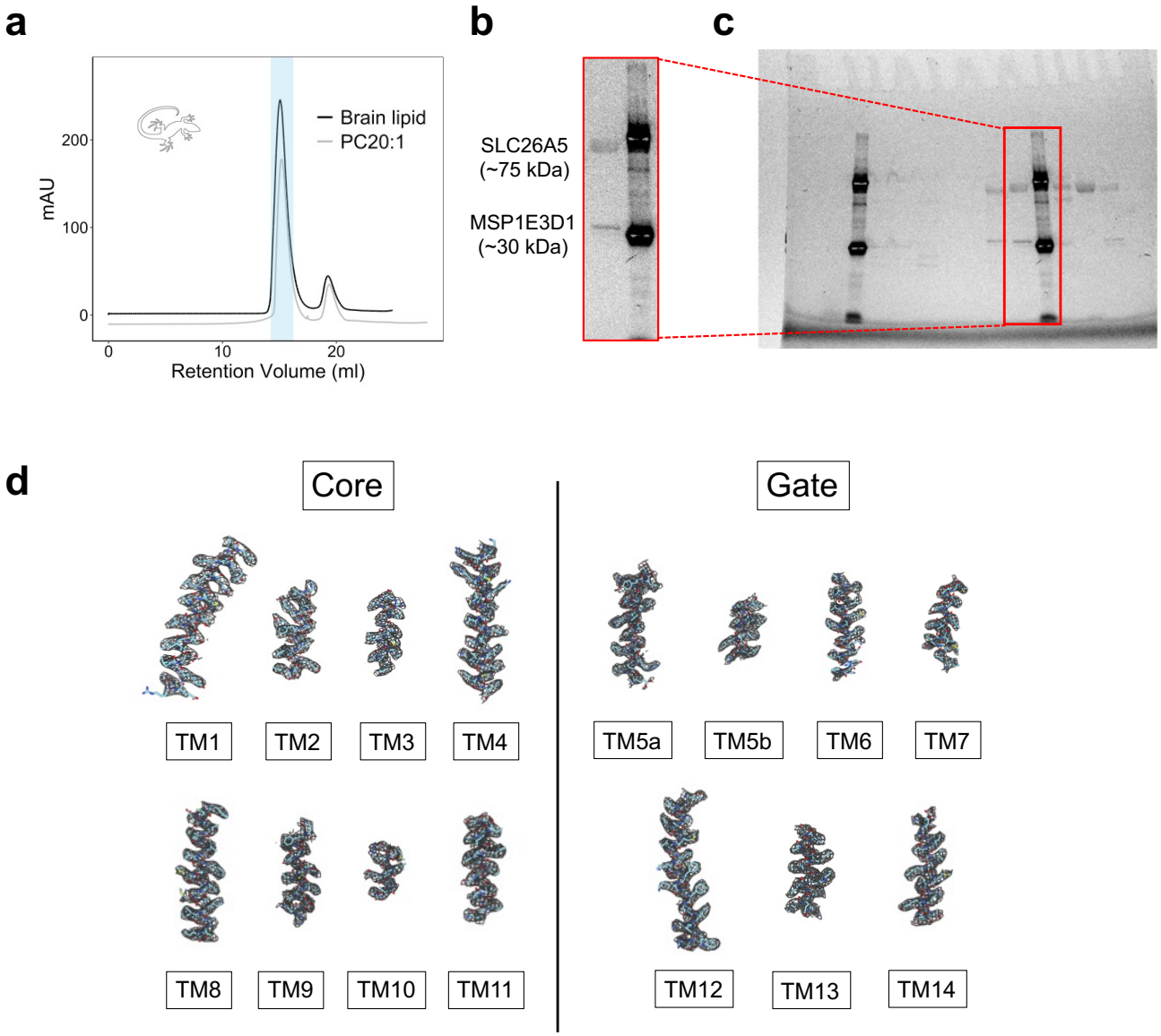

Supplementary Figure 5: Biochemistry of lizard SLC26A5. a) Size-exclusion chromatography (SEC) HPLC of purified lizard SLC26A5 in brain lipid and PC20:1 lipid composition nanodiscs (MSPE3D1), resulting in a monodisperse peak using a Superose 6 column. The peak was subsequently collected and concentrated for sample freezing. **b**) Only representative purification samples are shown for clarity. Lizard SLC26A5 monomer elutes at ~80 kDa (~160 kDa as a dimer), while MSPE3D1 elutes at ~30 kDa. **c**) The uncropped SDS-PAGE of lizard SLC26A5. The bands in the red rectangle correspond to lizard prestin. **d**) Density fit for the transmembrane region of lizard SLC26A5 in brain lipid nanodiscs.